Dynamics of floating wind turbine wakes in a wind tunnel setup

Ricardo Amaral[1], Felix Houtin-Mongrolle[2], Dominic von Terzi[1], Kasper Laugesen[3], Paul Deglaire[4], and Axelle Viré[1]

[1]Delft University of Technology, Wind Energy Section, Kluyverweg 1, 2629 HS Delft, Netherlands
[2]Siemens Gamesa Renewable Energy (SGRE), Prinses Beatrixlaan 800, 2595 BN Den Haag, Netherlands
[3]Siemens Gamesa Renewable Energy (SGRE), Borupvej 16, 7330 Brande, Denmark
[4]Siemens Gamesa Renewable Energy (SGRE), Avenue de l'Université C/O INSA Rouen - BP 08, 76800 Saint Étienne de Rouvray, France

Correspondence: Ricardo Amaral (r.pintoelisbaomartinsamaral@tudelft.nl)

Abstract. The wake of a laboratory-scale floating offshore wind turbine model is investigated under prescribed sinusoidal surge, sway, roll, pitch, and yaw motions, using large-eddy simulations coupled to an actuator-line model. The study aims to assess how the wake of a moving turbine evolves in a high blockage ratio wind tunnel, and to compare the results with the literature on full-scale models and experiments. The present work covers sinusoidal motions in five of the six floating offshore wind turbine degrees of freedom in a single study, and uses radial probes that sample circular two-dimensional cross-sections of the wake at several downstream positions instead of the commonly used linear probes. Two cases per degree-of-freedom are considered, corresponding to two distinct wake regimes: one with a low frequency and high amplitude, and one with a high frequency and low amplitude. The low-frequency/high-amplitude cases exhibit wake behavior close to the fixed-bottom case, as the prescribed frequency falls outside the high-energy spectral range naturally developed by the fixed-bottom wake. Conversely, the high-frequency/low-amplitude cases, whose prescribed frequency is within this high-energy range, produce strongly amplified perturbations, more irregular wake boundaries, earlier tip and root vortex trail expansion and merger, sharper turbulence intensity peaks, and faster wake recovery. The amplification is concentrated at the tip and root vortex trails, where the shear flow instability is strongest. An exception is the high-frequency surge case, which hampers wake recovery at the simulated frequency. Within the high-frequency/low-amplitude cases, prescribed motions with greater cross-stream components lead to higher wake recovery overall, and higher wake recovery gradient and cross-stream turbulence intensity in the near wake. Despite the high blockage ratio and wake confinement, all phenomena identified are consistent with the literature, confirming that the fundamental floating wind turbine wake dynamics are captured in this setup.

1 Introduction

In September 2024, Europe had 35 GW of installed offshore wind power capacity. This capacity is set to grow to 54 GW by 2030 (Costanzo et al., 2024). Most offshore wind turbines installed are fixed-bottom wind turbines, since they are more cost-competitive than floating offshore wind turbines (FOWTs) for water depths below 50-60 m (Cozzi et al., 2019; Barooni et al., 2023). However, harvesting wind energy in locations with water depths higher than 60 m, and more than 60 km away from the shore, has the potential to supply the world's total electricity demand several times by 2040 (Cozzi et al., 2019). At these depths, FOWTs are more cost-competitive, making them a viable technology for supporting the energy transition. As a result, floating offshore wind farms are already under operation, with 10 GW of capacity expected in Europe by 2030 (WindEurope, 2022).

In floating offshore wind farms, the interaction between the wakes of upstream turbines and downstream turbines affects both the wind farm energy yield and the loads that the turbines are subjected to. While established engineering wake models capture this interaction for fixed-bottom turbines (Jensen, 1983; Katic et al., 1986; Ainslie, 1988; Larsen et al., 2007; Larsen, 2009; Bastankhah and Porté-Agel, 2014), FOWTs are free to move and may be subjected to motions induced by the wind and sea. These motions act as upstream inflow perturbations, whose effects on the wake have so far not been captured by standard engineering wake models that do not intrinsically solve the time-varying frequency-dependent nature of the wake. As a consequence, a substantial amount of research has been conducted in recent years with the aim of understanding the factors driving FOWT wake dynamics.

It is now widely accepted that turbine wakes act as amplifiers of upstream perturbations. These amplified perturbations are the result of shear flow instabilities (Gupta and Wan, 2019) that are particularly excited under low turbulence and strong shear layers (Messmer et al., 2025), resulting in wake pulsation, wake meandering, and earlier tip and root vortex breakdown (Mao and Sørensen, 2018; Gupta and Wan, 2019; Li et al., 2022; Hodgson et al., 2023; Messmer et al., 2024; Mian et al., 2025; Messmer et al., 2025). The excitation of favorable wake modes is selective, depending on the frequency and amplitude of the perturbations, and leads to large-scale coherent structures that boost wake recovery and turbulence intensity in the wake (Mao and Sørensen, 2018; Gupta and Wan, 2019; Li et al., 2022; Hodgson et al., 2023; Messmer et al., 2024; Mian et al., 2025; Messmer et al., 2025). This results from shifting the streamwise position at which the wake recovery gradient increases sharply (Messmer et al., 2024), which coincides approximately with the point where the tip shear layers merge and the wake transitions to the far-wake (Kang et al., 2014; Messmer et al., 2024). The earlier breakdown of the tip vortex sheet triggered by the coherent structures appears to be the key event that leads to a steeper wake recovery, as the tip vortex sheet presence insulates the inner wake from the free stream, preventing net momentum entrainment (Medici, 2005; Lignarolo et al., 2015; De Cillis et al., 2020). Moreover, the coherent structures increase Reynolds shear stress gradients, particularly in the streamwise-lateral direction, which are found to be the key drivers of wake recovery (Messmer et al., 2025). Several studies suggest that wakes tend to amplify frequencies in the vicinity of a peak Strouhal number $St = fD/U_0 \approx 0.4$, where f is the prescribed motion frequency, D is the turbine diameter and U_0 is the free-stream velocity (Medici and Alfredsson, 2006; Chamorro and Porté-Agel, 2010; Chamorro et al., 2013; Okulov et al., 2014; Howard et al., 2015; Heisel et al., 2018; Gupta and Wan, 2019; Li et al., 2022; Hodgson et al., 2023; Messmer et al., 2024; Fontanella et al., 2024; Mian et al., 2025; Firpo et al., 2026). The amplification effects tend to be stronger in the range of 0.1-0.9 and are found to drop as the Strouhal number moves away from the peak value (Gupta and Wan, 2019; Li et al., 2022; Messmer et al., 2024; Mian et al., 2025).

The presence of free-stream turbulence in the inflow, akin to that of realistic inflows, is found to diminish the effects of the floating turbine motion in the wake. Free-stream turbulence intensity values as low as 1.5% accelerate the transition to the far-wake, and boost wake recovery, contributing as much as or more to the transition than the turbine movement for high enough values (Li et al., 2022, 2024; Pagamonci et al., 2025; Messmer et al., 2025). The effect of turbulence is twofold. First, it greatly improves mixing between the wake and the free-stream, thus boosting momentum entrainment and accelerating the wake recovery (Mian et al., 2025). Second, it dissipates the coherent wake structures caused by the floating turbine motion, thus attenuating their wake recovery benefits (Li et al., 2024; Pagamonci et al., 2025; Mian et al., 2025; Messmer et al., 2025; Firpo et al., 2026). Beyond turbulence intensity values of about $I \approx 5\%$, the benefits of the prescribed motion to the wake recovery are found to be negligible (Messmer et al., 2025). This is nevertheless dependent on the turbulent time scales, as turbulent flows that contain more energy in the Strouhal number range of $0.3-0.7$ stimulate the transition to the far wake by breaking down the near-wake (Hodgson et al., 2023).

Floating turbine motions with a cross-stream component are found to be the most beneficial for wake recovery, with the benefits extending up to higher values of turbulence intensity (Fontanella et al., 2024, 2025; Messmer et al., 2025). However, when the turbine is subjected to stochastic sea-states that introduce combined platform motions, there may be no appreciable benefit to wake recovery (Fontanella et al., 2025).

The present study covers motions in the surge, sway, roll, pitch and yaw degrees of freedom. In order to accommodate many degrees of freedom and analyses, two cases per degree-of-freedom are considered, corresponding to two distinct wake regimes: one with a low Strouhal number and high amplitude, and one with a high Strouhal number and low amplitude. Two-dimensional radial probe data are used to assess the downstream evolution of the wake recovery, recovery gradient, turbulence intensity and wake velocity spectral components by converting the data from each of the probes into a single number at each downstream position. This conversion is achieved through spatial averaging and allows for a more practical comparison of all simulated cases. The velocity perturbation amplification factors are used to assess the wake velocity spectral components against the initial prescribed motion velocity perturbations, similarly to what was done in Li et al. (2022). The present study also analyzes the evolution of the wake morphology using Q-criterion surfaces and a method based on the standard deviation of the velocity magnitude to quantify the thickness of the tip and root vortex trails in the wake, while capturing the downstream position at which they merge.

This investigation builds on recent experimental and CFD studies carried out in the Politecnico di Milano wind tunnel on the 1:75-scaled version of the DTU 10 MW reference wind turbine (Fontanella et al., 2021a, b; Bergua et al., 2023; Cioni et al., 2023; Fontanella et al., 2024, 2025; Pagamonci et al., 2025; Cioni et al., 2025; Firpo et al., 2026), and aims to provide a complementary analysis of the wake of the same turbine model in the same wind tunnel, leveraging the detail that large-eddy simulations and the actuator-line model can offer. The three key features of this study are: (1) it compares surge, sway, roll, pitch and yaw motions; (2) it uses data sampled from radial probes that cover circular two-dimensional sections of the wake at several downstream positions, instead of the commonly used linear probes; and (3) it analyzes the wake in terms of recovery, recovery gradient, turbulence intensity, wake velocity spectral components, morphology, and tip and root vortex trail evolution and merger. While the overarching conclusions are broadly consistent with the existing literature on floating wind turbine wakes and are not novel, the simultaneous coverage of points (1), (2) and (3) has not been carried out on the scaled version of the DTU 10 MW reference wind turbine in the Politecnico di Milano wind tunnel, especially in terms of the tip and root vortex trail analysis, to the authors' best knowledge. The objective of this study is three-fold. First, it identifies differences in the two wake regimes resulting from each pair of Strouhal number and amplitude, as well as differences across degrees of freedom.

These differences are linked to the well-known frequency-dependent wake behavior that favors cross-stream perturbations, identified in the literature for full-scale models and experiments. Second, it pinpoints instances where the wind tunnel setup and high blockage ratio may have interfered with the wake evolution. Third, it concludes that, despite interference in the wake, the wake behavior in the wind tunnel under high blockage ratio is broadly consistent with the findings in the literature for less constrained setups.

The authors were previously involved in the IEA task OC6 Phase III (Fontanella et al., 2021a, b; Bergua et al., 2023; Cioni et al., 2023) and hence, the numerical setup and case definition were largely based on the IEA task definition. The surge and pitch cases were defined exactly as in the IEA task. The sway cases were performed at the same pairs of Strouhal number and amplitude as the surge cases. Similarly, the roll and yaw cases were performed at the same pairs of Strouhal number and amplitude as the pitch cases. The objective was to provide the same perturbations as surge for the translational degrees of freedom, and as pitch for the rotational degrees of freedom. No turbulence was considered to highlight the wake dynamics induced exclusively by the turbine motion.

2 Methodology

2.1 Numerical framework

Studying wind turbine wakes in detail requires the use of high-fidelity techniques at high mesh resolutions to capture the small scales that may be decisive in driving the wake evolution. Large-eddy simulations (LES) are a suitable method in which the Navier-Stokes (NS) equations are spatially filtered with a filter size within the inertial range. For a constant density fluid, the filtered NS equations are:

$$\frac{\partial \widetilde{u}_j}{\partial t} + \frac{\partial \widetilde{u}_i \widetilde{u}_j}{\partial x_i} = -\frac{1}{\rho}\frac{\partial \widetilde{p}}{\partial x_j} + \frac{1}{\rho}\frac{\partial \tau^{\mathrm{r}}_{ij}}{\partial x_i} + \nu \frac{\partial^2 \widetilde{u}_j}{\partial x_i \partial x_i} + \frac{\widetilde{f}_j}{\rho} \qquad \text{and} \qquad \frac{\partial \widetilde{u}_i}{\partial x_i} = 0, \tag{1}$$

where Einstein's notation is used, $\widetilde{\cdot}$ is the filtering operator, u is the velocity vector, p is the pressure, ν is the kinematic viscosity, ρ is the density and f is the external volume forces. The subgrid scale stress tensor τ^{r}_{ij} was based on the dynamic Smagorinsky model (Germano et al., 1990). The turbine was modeled with an actuator-line model (ALM) (Sorensen and Shen, 2002). The equations were solved using the YALES2 flow solver (Moureau et al., 2011), which is a massively parallel finite-volume solver specifically tailored for LES. YALES2 relies on a central fourth-order numerical scheme for spatial discretization, and a method similar to the fourth-order Runge-Kutta method for the time integration (Kraushaar, 2011). While the discretization is strictly fourth-order on Cartesian grids, this order of convergence can decrease on tetrahedral grids with poor cell quality. YALES2's ALM implementation is described in Houtin-Mongrolle (2022). The necessity of fairly high-order numerics to ensure the proper transport of fine vortical structures, in the context of the ALM, was demonstrated in Benard et al. (2018), where the authors advise a minimum grid resolution at the rotor and wake regions, and actuator line discretization in unstructured meshes of $D/\Delta x \approx 66$ to ensure adequate numerical accuracy.

2.2 Wind turbine model and floating degrees of freedom

The simulation setup largely reproduced the one from the IEA task OC6 Phase III (Bergua et al., 2023; Cioni et al., 2023). The domain in the simulations reproduced the cross-section of the Politecnico di Milano wind tunnel and the wind turbine model used in the experiment. The wind turbine model was a laboratory-scale DTU 10 MW wind turbine (Bak et al., 2013; Bayati et al., 2017; Fontanella et al., 2021b) that was scaled-down from the original full-scale DTU 10 MW using the length and velocity scaling factors $\lambda_L = D_{\mathrm{DTU10MW}}/D_{\mathrm{Model}} = 75$ and $\lambda_{U_\mathrm{R}} = U_{\mathrm{R}_{\mathrm{DTU10MW}}}/U_{\mathrm{R}_{\mathrm{Model}}} = 3$, where D is the turbine diameter and U_R is the rated wind speed. Moreover, it was designed to have the same thrust coefficient curve as the DTU 10 MW at lower rated wind speed, by means of low-Re number airfoils (Bayati et al., 2017), where Re is the Reynolds number. Some standard features of the model can be seen in Table 1. The power and thrust coefficients were computed from the torque and thrust values measured in the IEA task OC6 Phase III.

Fig. 1 (a) shows the simulated components (blades only) in perspective, where the rotor rotates clockwise. The turbine configuration used in the CFD simulations was the same as the one used in the IEA task OC6 Phase III and this can be seen in Fig. 1 (b). No tower, nacelle, or hub were simulated but the dimensions of these components are shown in Fig. 1 (b) as simple black lines because they were taken into account when prescribing motions in rotational degrees of freedom (DOFs). The setup dimensions are shown in Table 2, where z_{rc} is the rotor center height. A difference in rotor center height between translational and rotational cases is present, as per the experimental setup. For the translational case configuration, it suffices to only provide the rotor center height in Table 2, since the velocity induced by the translational prescribed motions, such as surge or sway, is the same for every point in the rotor. For the rotational case configuration, all the dimensions are relevant and are provided in Table 2. Two points are worth noting in this setup. First, the rotor tilt and the angle α cancel out so that the rotor is perpendicular to the free-stream velocity, at the starting position. This was done to isolate the prescribed motion effects from the rotor tilt effects. Second, the turbine is closer to the top wall than to the bottom wall, as per the experimental setup.

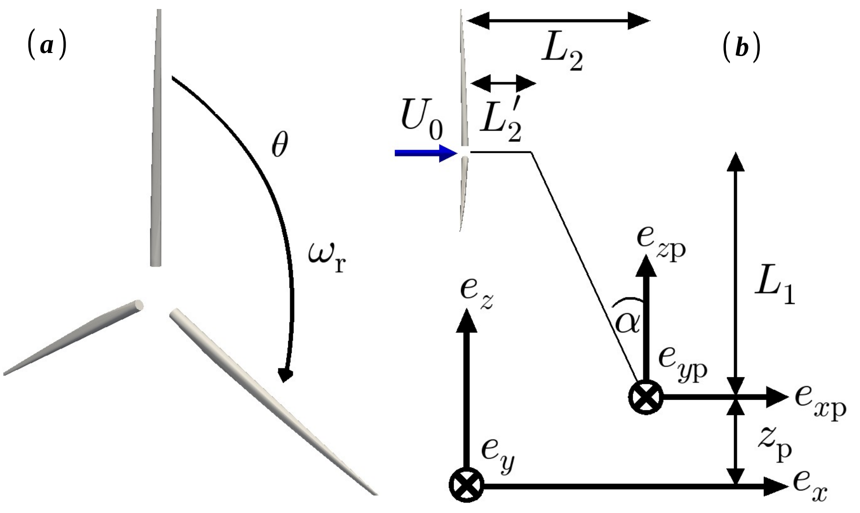

Figure 1. Simulated components (blades only) in perspective (a) and initial turbine setup with reference frames (b).

Table 1. Turbine characteristics and rated operating parameters.

Rotor diameter	Hub diameter	Blade length	Rotor tilt	Rated wind speed	Rated rotor speed	Tip-speed ratio	Power coefficient	Thrust coefficient
D	D_{H}	L_{b}	-	U_{R}	Ω_{R}	λ	C_P	C_T
2.381 m	0.178 m	1.102 m	5 deg	4 ms^{-1}	240 rpm	7.476	0.486	0.859

Table 2. Turbine setup dimensions.

	z_{p}	L_1	$L_{2'}$	L_2	α	$z_{\mathrm{rc}} = z_{\mathrm{p}} + L_1$
Translation	-	-	-	-	5 deg	2.086 m
Rotation	0.730 m	1.458 m	0.139 m	0.267 m	5 deg	2.188 m

Two reference frames can be identified in Fig. 1 (b). The global reference frame is the frame $\boldsymbol{e_x}$-$\boldsymbol{e_y}$-$\boldsymbol{e_z}$ which is centered at the point $(0,0,0)$ and is fixed. $\boldsymbol{e_y}$ follows the right-hand rule. The initial coordinates of the rotor center in this frame are $(0,0,z_{\mathrm{rc}})$. The surge, sway and heave motions are, respectively, translations in the $\boldsymbol{e_x}$, $\boldsymbol{e_y}$ and $\boldsymbol{e_z}$ directions and are defined relative to the global reference frame. The prescribed reference frame is the frame $\boldsymbol{e_{xp}}$-$\boldsymbol{e_{yp}}$-$\boldsymbol{e_{zp}}$ which is centered at the fictitious tower bottom and translates with the turbine. $\boldsymbol{e_{yp}}$ follows the right-hand rule. The roll, pitch and yaw motions are, respectively, the rotations about the $\boldsymbol{e_{xp}}$, $\boldsymbol{e_{yp}}$ and $\boldsymbol{e_{zp}}$ directions. All the aforementioned motions are defined in the floating foundation context and can be visualized in Fig. 2. Heave was not included to avoid overcrowding the figure and because it was not simulated.

The prescribed motions in every DOF were of the form:

$$p = \pm A_{\mathrm{p}} \sin(\omega_{\mathrm{p}} t), \tag{2}$$

where p is the corresponding prescribed motion (in length units for translational cases and angle units for rotational cases), A_{p} is the prescribed motion amplitude, and $\omega_{\mathrm{p}} = 2\pi f_{\mathrm{p}}$ is the prescribed motion angular frequency.

The cases in this study are defined by the prescribed Strouhal number St_{p} and the normalized amplitude A^*_{p}, which are defined below. The Strouhal number is the normalized or reduced frequency defined by:

$$St_{\mathrm{p}} = \frac{f_{\mathrm{p}} D}{U_0}, \tag{3}$$

where f_{p} is the prescribed motion frequency, D is the turbine diameter and U_0 is the free-stream velocity.

For the translational DOFs, the normalized amplitude of prescribed motion is defined by:

$$A^*_{\mathrm{p}} = \frac{A_{\mathrm{p}}}{D}, \tag{4}$$

where A_{p} is the prescribed motion amplitude, the subscript "p" stands for "prescribed", and the superscript "*" indicates that a quantity was normalized by D (e.g., $x^* = x/D$).

For the rotational DOFs, the amplitude of the prescribed motions is an angle, which makes it difficult to compare with the translational DOFs. Thus, it is useful to provide the amplitude that the prescribed motion induces at the rotor center A^*_{prc}:

$$A^*_{\mathrm{prc}} = \frac{A_{\mathrm{prc}}}{D}, \tag{5}$$

where the subscript "rc" stands for "rotor center". For the translational DOFs, $A^*_{\mathrm{prc}} = A^*_{\mathrm{p}}$. For the rotational DOFs, $A^*_{\mathrm{prc}} = A_{\mathrm{p}} L_{\mathrm{rot}}/D$, where L_{rot} is the distance from the rotor center (roll and pitch cases) or blade tip (yaw cases) to the rotation axis.

All the quantities used in the study are normalized, i.e., made non-dimensional, unless otherwise indicated. Hence, the adjective "normalized" will be dropped after the quantity is defined, to avoid unnecessary repetitions.

All the prescribed motion amplitudes were defined relative to the initial turbine setup in Fig. 1 (b). The prescribed motion capability was implemented in YALES2 and the blade kinematics validation can be seen in Appendix A.

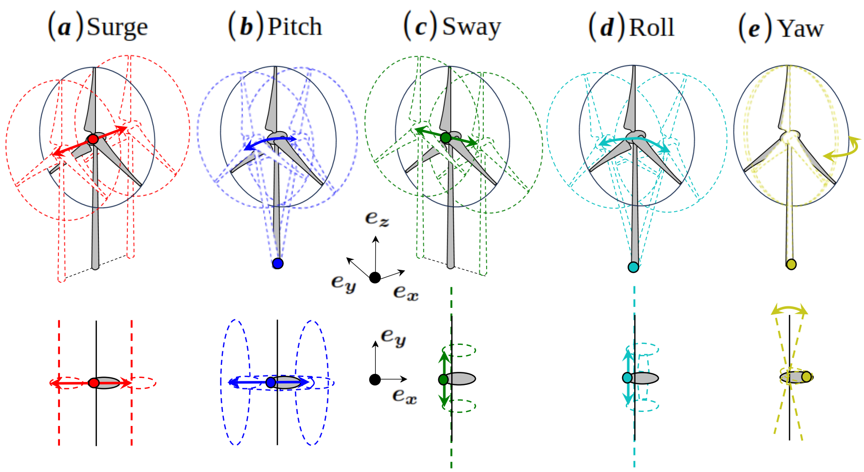

Figure 2. Floating foundation DOFs and the motion they induce on the turbine.

2.3 Case definition

According to the conditions of the IEA task OC6 Phase III, the turbine was modeled as rigid, was operated near rated conditions, the rotor speed was constant ($\Omega_{\mathrm{r}} = 240$ rpm), the blades were pitched at the optimal value of 0 deg, and the free-stream velocity was equal to the rated wind speed of the turbine ($U_0 = U_{\mathrm{R}} = 4\ \mathrm{ms}^{-1}$). The turbine was operated under constant rotor speed to isolate the effects of the prescribed motion. This simplification is not expected to have a large impact, since the rotor was operated near rated conditions. While in the IEA task OC6 Phase III, the inflow was turbulent with a turbulence intensity of around 2%, the inflow was laminar in the simulations performed in this study. This simplification was done to focus the analysis on the unsteady wake effects induced by the turbine motion, similarly to what was done by Messmer et al. (2024) and Mian et al. (2025), although it should be acknowledged that realistic inflows are turbulent and that even turbulence intensity levels as low as 1.5% (Li et al., 2022; Pagamonci et al., 2025; Messmer et al., 2025) can have a large impact on the wake dynamics.

Furthermore, in the IEA task OC6 Phase III, the flow had boundary layers near the walls. These were absent in the performed simulations, given that the walls were modeled as slip walls. This simplification slightly reduces the effective blockage in the simulations but the impact on the wake dynamics is expected to be small, given that the largest contribution to the blockage comes from the turbine itself, resulting in a blockage ratio of around 8.46%. Hence, it was decided to use slip walls, thereby reducing the computational cost. Lastly, the time-averaged inflow in the IEA task OC6 Phase III was approximately uniform in the rotor region, which was the goal. Hence, no shear was considered in the simulations. A summary of the operating conditions and boundary conditions is provided in Table 3.

Table 3. Operating conditions and boundary conditions.

Free-stream velocity	Inflow	Blade stiffness	Blade pitch	Rotor speed	Wall boundary condition	Blockage ratio
U_0				Ω_r		
4 ms^{-1}	Laminar, no shear	Rigid	0 deg	Constant, 240 rpm	Slip wall	8.46%

The simulated cases are described in Table 4 showing the dimensional prescribed motion frequency f_p, the prescribed motion Strouhal number St_p, the dimensional prescribed motion amplitudes A_p, and the corresponding prescribed motion amplitudes at the rotor center A^*_prc. The cases are named using the first two letters of the prescribed motion DOF (e.g., "Su" for surge). These letters are followed by either "LS" or "HS" standing for "low-St_p/high-A^*_p" or "high-St_p/low-A^*_p", respectively. Two cases per DOF were chosen from the IEA task OC6 Phase III, one with a low St_p and high A^*_p, and vice versa. Only two cases per DOF were chosen because the goal was to cover many DOFs, while limiting the computational cost. The prescribed motion amplitude at the rotor center is in general ten times larger for the low-St_p/high-A^*_p cases, than for the high-St_p/low-A^*_p cases. The cases were initially chosen in this way because it was hypothesized that the prescribed motion impact on the rotor apparent wind speed would be the main driver of wake dynamics. However, as reported in the literature, the wake behavior is highly frequency dependent, with the amplitude having an important but secondary role.

The surge and pitch cases were performed at the same frequencies and amplitudes as some of the cases found in the IEA task OC6 Phase III. These frequency and amplitude values were scaled down from the corresponding values that the full-scale DTU 10 MW would be subject to in conditions representative of different FOWT support structures under near-rated conditions (Bergua et al., 2023), using the length and velocity scaling factors of the model described in Section 2.2. The sway cases were performed at the same pairs of Strouhal number and amplitude as the surge cases. Similarly, the roll and yaw cases were performed at the same pairs of Strouhal number and amplitude as the pitch cases. The objective was to provide the same perturbations as surge for the translational DOFs, and as pitch for the rotational DOFs. Both the dimensional and non-dimensional values of frequency and amplitude are provided in Table 4 for clarity.

Table 4. Case definition. The nomenclature is as follows: "FB" stands for "fixed-bottom"; "Su" stands for "surge"; "Pi" stands for "pitch"; "Sw" stands for "sway"; "Ro" stands for "roll"; "Ya" stands for "yaw"; "LS" stands for "low-St_{p}/high-A^{*}_{p}" and "HS" stands for "high-St_{p}/low-A^{*}_{p}".

Case	DOF	f_{p} [Hz]	St_{p} $[-]$	A_{p}	A^{*}_{prc} $[-]$
FB	Fixed-bottom	0	0	0	0
SuLS	Surge	0.125	0.0744	0.125 m	0.0525
SuHS	Surge	2.000	1.1905	0.008 m	0.0034
PiLS	Pitch	0.125	0.0744	3.0 deg	0.0326
PiHS	Pitch	2.000	1.1905	0.3 deg	0.0033
SwLS	Sway	0.125	0.0744	0.125 m	0.0525
SwHS	Sway	2.000	1.1905	0.008 m	0.0034
RoLS	Roll	0.125	0.0744	3.0 deg	0.0321
RoHS	Roll	2.000	1.1905	0.3 deg	0.0032
YaLS	Yaw	0.125	0.0744	3.0 deg	0.0268
YaHS	Yaw	2.000	1.1905	0.3 deg	0.0027

2.4 Computational setup

The rotor was placed in a computational domain of dimensions $19D \times 5.8D \times 1.6D$ and centered at a distance of $5D$ from the domain inlet. The domain reproduced the cross-section of the boundary layer test section of the Politecnico di Milano wind tunnel, whose dimensions are 35 m long x 13.84 m wide x 3.84 m high. The domain was made longer in the wind direction, so as to place the turbine farther away from the inlet and the outlet. The mesh was unstructured and composed of around 318 million tetrahedral elements. Figures 3 (a) and (b) show a transversal and longitudinal slice of the domain depicting its dimensions and refinement regions with the corresponding mesh resolution $D/\Delta x$, where Δx is the cell size. $D/\Delta x$ is the inverse of the non-dimensional cell size and represents how many actuator points would exist in a rotor diameter, given the cell size of the point in question. Two refinement levels were used, the wake refinement and the background refinement. The wake refinement level is the high-refinement region with an average and maximum cell size in the vicinity of the rotor equal to 2.5×10^{-2} m and 3.2×10^{-2} m, respectively. This region was cylindrical with a radius and length of approximately $1D$ and $8.5D$. The number of actuator points in the rotor was set according to the maximum cell size and yielded 66 actuator points per diameter. The ratio of the smearing length scale and the maximum cell size in the vicinity of the rotor was set to $\epsilon/\max(\Delta x) = 2$ (Troldborg et al., 2009). The cell size grew at a rate of 1.07 from the wake refinement to the background refinement at the domain boundaries. The background refinement had a minimum resolution of $D/\Delta x = 9$.

The simulations were carried out with a variable time step that was set such that $\mathrm{CFL} \leq 0.9$ for every cell and time instant, where $\mathrm{CFL} = ||u||\Delta t/\Delta x$ is the Courant–Friedrichs–Lewy number. The simulations were run for 64 s and the statistics were taken in the last 32 s (see Appendix B for the time convergence validation). The Reynolds number at the airfoil sections was

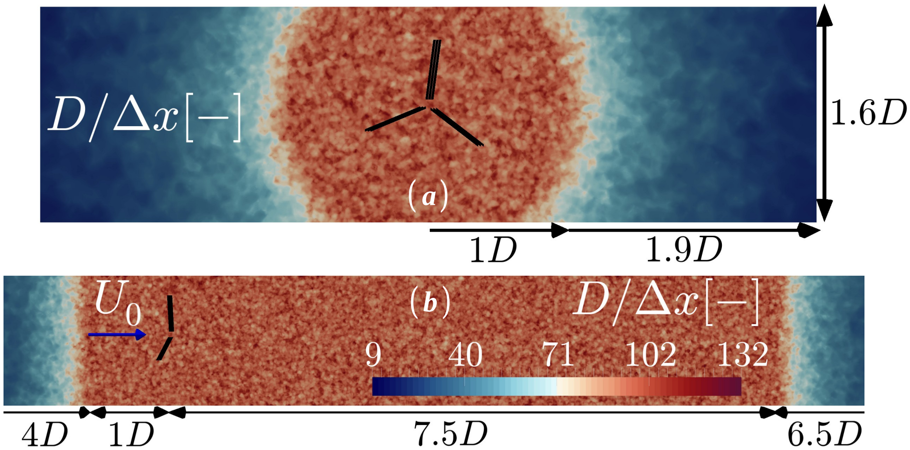

Figure 3. Transversal slice of the domain (a) and longitudinal slice of the domain (b) showing the mesh resolution. The inlet and outlet were trimmed in (b).

found to be within 5% of the design value for the fixed-bottom case in the most loaded blade region, between $s \approx 30\,\%$ and $s \approx 97\,\%$, where s is the spanwise position.

A comparison with experimental loads results for the surge and pitch cases is included in the Appendix C. The agreement between simulations and experiments was not exact, but there were modeling limitations on the simulation side, as well as technical limitations and uncertainties on the experimental side that may have contributed to the mismatch. Overall, the simulation setup was considered acceptable given that the wake behavior is mostly driven by the operating point of the turbine, the thrust coefficient and the floating turbine motion. Similarly to the experimental cases, the turbine operated near rated conditions in the C_P-maximizing region. The mean thrust coefficient was, at most, 8% above or below the experimental values. The thrust amplitude of cases SuLS and PiLS was, at most, 10% above or below the experimental values. The thrust amplitude of cases SuHS and PiHS exhibited larger discrepancies, which may be attributed to the higher uncertainty in the measurements associated with the inertial loads (Bergua et al., 2023), and the prescribed amplitude mismatch between the experimental data of PiHS (0.26 deg) and the load case definition (0.3 deg).

2.5 Data extraction

The wake was characterized by extracting the time series of the three flow field velocity components at several streamwise positions, by means of radial probes, such as those shown in Fig. 4. Each radial probe was composed of 98 linear sub-probes dispersed azimuthally with a uniform angular spacing, and discretized into 41 points in the radial direction. The number of sub-probes and their points represented a trade-off between spatial resolution and data size. The radial probe radius was $1.25D$ with a radial resolution of about 33 points per diameter, and a minimum azimuthal resolution at the rotor perimeter of about

31 points per diameter. The time series were acquired at each point in the probe. The probes' axes were aligned with the initial rotor axis throughout the simulation and did not move with the turbine.

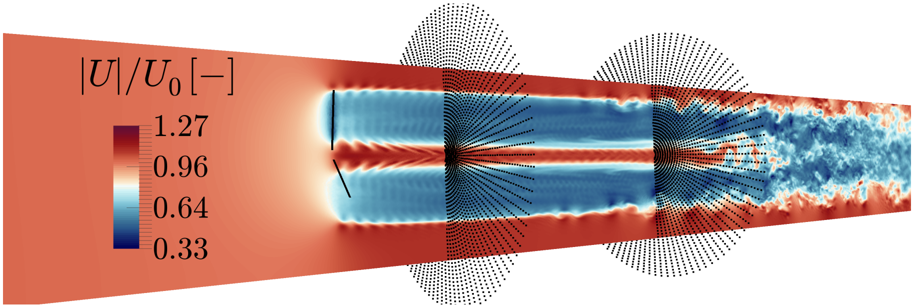

Figure 4. Two radial probes superimposed on a longitudinal domain slice. The probes are shown as black dots. The slice was colored by the instantaneous streamwise velocity contours at $t/T_{\mathrm{p}} = 4$ for the SuLS case, where $T_{\mathrm{p}} = 1/f_{\mathrm{p}}$.

3 Results

Multiple analyses were carried out in this section with the goal of identifying differences in the simulated cases. These analyses were based on the data extracted from the radial probes presented in the previous subsection, as well as Q-criterion surfaces and two-dimensional longitudinal slices of the velocity field. Each analysis is presented in a separate subsection and consists of the following:

1. Wake recovery. The velocity field data from the radial probes are first used to visualize transversal slices of the wake at several downstream positions to ascertain the impact of the prescribed motions on the time-averaged streamwise velocity field. Then, the time-averaged streamwise velocity field is spatially averaged in a region delimited by the rotor perimeter, yielding a single average value for each downstream position. The wake recovery profile of each case is then easily visualized and compared, by plotting the average values against the downstream position.

2. Turbulence intensity. This subsection follows the same principles as the "Wake recovery" subsection. First, the streamwise turbulence intensity is visualized at several transversal slices of the wake. Second, both the streamwise and cross-stream turbulence intensity values are spatially-averaged at each downstream position, and their evolution is assessed.

3. Frequency contents. The downstream evolution of the frequency contents of the wake is evaluated. First, the cross-stream velocity field spectra are calculated for each point in each radial probe. Then, these data are spatially averaged, yielding an average wake spectrum per downstream position. Afterwards, the spectral component at the prescribed motion frequency is extracted from the average wake spectrum and compared with the initial prescribed motion velocity perturbation. The ratio of both quantities was designated as velocity perturbation amplification factor and quantifies the degree to which the initial prescribed motion velocity perturbation is amplified by the wake, with the objective of inferring which DOFs

and which frequencies are the most critical. This subsection ends with a spatial analysis of the wake regions exhibiting the greatest amplification of the prescribed motion. This is assessed from the radial probes by plotting the cross-stream velocity spectral component at the prescribed motion frequency over transversal wake slices.

4. Tip and root vortex trail. This subsection starts with a visualization of the effect that the prescribed motion has on the wake, and more specifically on the tip vortices, using Q-criterion surfaces. The visualization is followed by a more analytical approach that is based on longitudinal slices of wake, and in which the wake slices are colored using the standard deviation of the velocity magnitude. This quantifies the variability of the velocity field magnitude, where a higher variability is used as a proxy for the tip and root vortex trails in the wake. Afterwards, the thickness of the tip and root vortex trails is computed across the slices to evaluate their evolution and to identify the downstream position at which the trails merge for each case. The section ends with the analysis of the evolution of the cross-stream velocity spectra in the tip vortex trail.

3.1 Wake recovery

The first question that was investigated was the effect of the prescribed motion on the time-averaged wake and the consequences on the wake recovery. As a result, the normalized time-averaged streamwise flow velocity $<U_x>/U_0$ was examined at the radial probes, where $<\cdot>$ denotes the time average. The streamwise evolution of $<U_x>/U_0$ can be seen in Fig. 5 for several cases. The black dashed circle indicates the rotor perimeter. The black region on the top of each contour corresponds to the upper wall. Each row represents one downstream position while each column represents one case. The smooth plots were obtained via linear interpolation.

Looking at the fixed-bottom case, the time-averaged wake expanded steadily downstream while preserving the circular shape. This was a pattern that was observed for the SuLS, SwLS and SuHS cases, but not for the SwHS and PiHS cases, which developed more irregular edges. Although not shown, all of the low-St_p/high-A^*_p cases behaved similarly to the fixed-bottom case, while all of the high-St_p/low-A^*_p cases (except the SuHS case) behaved similarly to the SwHS and PiHS cases. These results suggest that exciting the wake at the simulated high-St_p/low-A^*_p pair leads generally to more destabilization at its outer boundary than the fixed-bottom case and the simulated low-St_p/high-A^*_p pair. The different behavior is somewhat expected, given the well-known frequency-dependent response of the wake to upstream perturbations. However, the Strouhal number of the high-St_p/low-A^*_p cases ($St_\mathrm{p} = 1.1905$) is outside the most favorable range of 0.1-0.9 reported in the literature. An explanation for the stronger destabilization observed in the high-St_p/low-A^*_p cases is provided in Section 3.3.

Comparing the wake of the SuHS case to the wakes of the SwHS and PiHS cases suggests that exciting the wake in a cross-stream direction (i.e., all DOFs but surge) leads to more destabilization than exciting the wake exclusively in the streamwise direction (i.e., surge), as also observed by Fontanella et al. (2024, 2025) and Messmer et al. (2025).

In order to compare the cases in a practical way, the values of some physical quantities were spatially averaged over the area between the hub and the rotor radius for each radial probe. The hub area was excluded to limit the impact of the absence of the

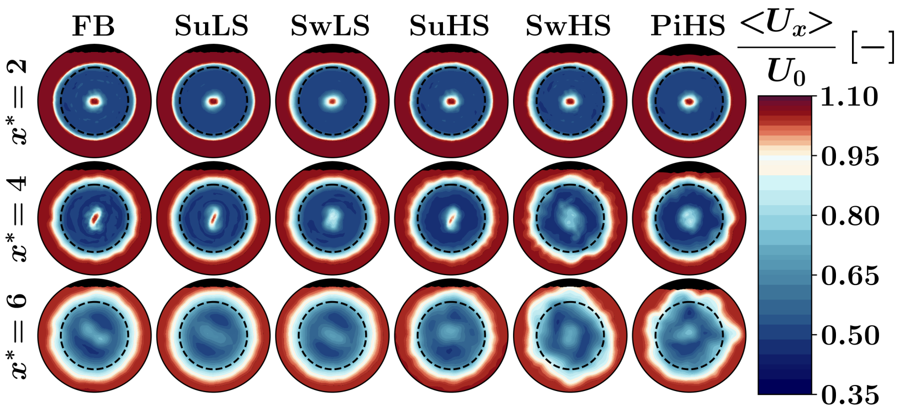

Figure 5. Time-averaged streamwise velocity over the radial probes at several streamwise positions. The black region corresponds to the upper wall. The black dashed circle delimits the rotor perimeter.

nacelle. For a general variable X, the spatial averaging was computed as:

$$\overline{X} = \frac{\int_0^{2\pi} \int_{r_\mathrm{h}}^{r_\mathrm{r}} X \, r dr d\theta}{\int_0^{2\pi} \int_{r_\mathrm{h}}^{r_\mathrm{r}} r dr d\theta}, \tag{6}$$

where $\overline{}$ denotes the spatial average, r_r is the rotor radius and r_h is the hub radius. This was done in this section for $<U_x>/U_0$ and the result was designated as wake recovery.

The wake recovery increment due to the prescribed motion was defined as the difference in wake recovery relative to the fixed-bottom case:

$$\Delta_\mathrm{FB} = \frac{\overline{<U_x>}}{U_0} - \frac{\overline{<U_x>}}{U_0}\bigg|_\mathrm{FB}, \tag{7}$$

and was used to quantify the effect of the prescribed motion on the wake recovery. Positive values of this quantity indicate that the wake recovery value is higher than that of the FB case for a given downstream position, and vice-versa.

Similarly, the wake recovery gradient increment due to the prescribed motion was estimated by the taking the gradient of Equation 7 and normalizing it by $1/D$:

$$D\frac{\partial \Delta_\mathrm{FB}}{\partial x} = \frac{D}{U_0}\left(\frac{\partial\overline{<U_x>}}{\partial x} - \frac{\partial\overline{<U_x>}}{\partial x}\bigg|_\mathrm{FB}\right), \tag{8}$$

where the gradient was calculated using forward finite differences. This represented the difference in how fast the wake recovered as it moved downstream, when compared to the FB case. Positive values of this quantity indicate that the wake was recovering faster than the FB case for a given downstream position, and vice-versa.

Figure 6 shows (a) the wake recovery, (b) the wake recovery increments and (c) the wake recovery gradient increments for several streamwise positions. The wake recovery increments and the wake recovery gradient increments are both absolute differences between physical quantities measured in percentage, hence they are also measured in percentage. The fixed-bottom case is shown in black, the high-St_p/low-A^*_p cases are shown in solid lines, and the low-St_p/high-A^*_p cases are shown in dashed lines. Figure 6 (a) shows that the wake recovery onset (i.e. minimum value of wake recovery) for almost all cases is located at $x^* = 3$, with the exception of cases SwHS and RoHS, whose onset is located at $x^* = 2$. It is worth noting that this difference in recovery onset position could be due to the relatively large radial probe spacing (equal to D), and that the actual difference in onset between the cases may be lower.

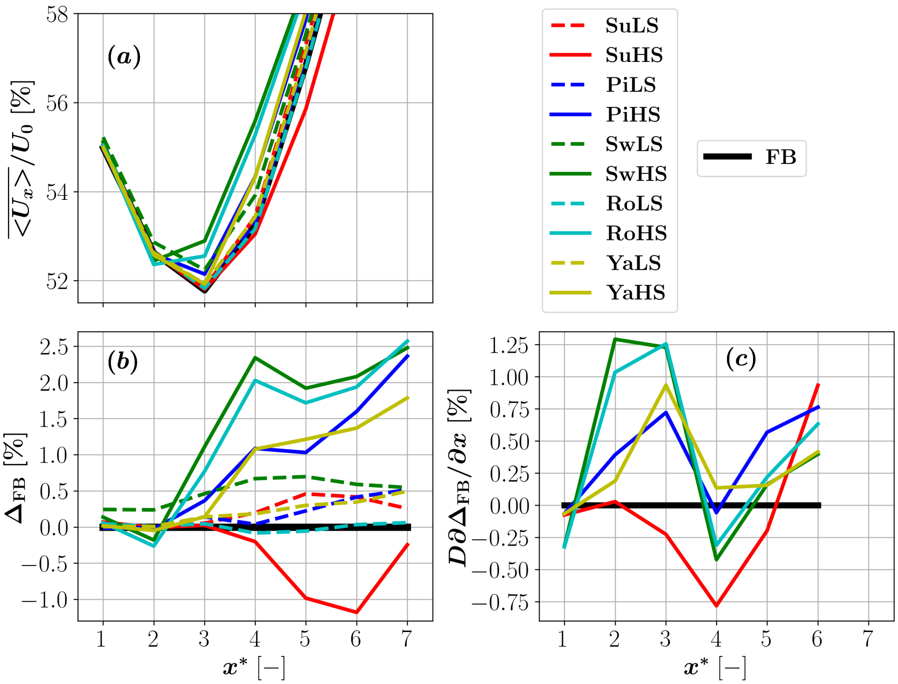

Figure 6. Evolution of the wake recovery (a), wake recovery increments (b) and wake recovery gradient increments for the high-St_p/low-A^*_p cases (c). The wake recovery increments and wake recovery gradient increments are absolute differences relative to the fixed-bottom case. The fixed-bottom case is shown in black, the high-St_p/low-A^*_p cases are shown in solid lines, and the low-St_p/high-A^*_p cases are shown in dashed lines.

Figure 6 (b) provides a clearer view as to which cases were more beneficial for the wake recovery. Almost all cases displayed positive wake recovery increments, meaning that the wake recovery was stronger than that of the fixed-bottom case, with the exception of the SuHS case that seemed to hamper the recovery between $x^* = 4$ and $x^* = 7$. Overall, the wake recovery increments from the prescribed motions were present but were small compared to the increments observed by Messmer et al. (2024), which were of the order of 10% at $x^* = 6$ in absolute difference. Two factors may have contributed to this. First, the simulated Strouhal numbers ($St_\mathrm{p} = 0.0744$ and $St_\mathrm{p} = 1.1905$) were both outside the most favorable range identified in the literature (0.1-0.9). Second, Fontanella et al. (2024) observed that the mean wake velocity of the same turbine in the same wind tunnel under surge, pitch, yaw, coupled surge-sway and coupled roll-pitch motions at several St_p and A^*, including $St_\mathrm{p} = 0.6$, was comparable to that of the fixed-bottom case at $x^* = 3$ and $x^* = 5$. The consistency of the low impact on the wake recovery in this experiment suggests that the wind tunnel blockage may have also played a role in hindering the wake recovery.

The high-St_p/low-A^*_p cases generally exhibited higher wake recovery increments than the low-St_p/high-A^*_p cases, a fact that is likely related to the frequency-dependent wake behavior and higher wake destabilization observed for most of the high-St_p/low-A^*_p cases in Fig. 5. Nevertheless, the low-St_p/high-A^*_p cases led, in general, to higher wake recovery than the fixed-bottom case.

Within the high-St_p/low-A^*_p cases, between $x^* = 4$ and $x^* = 6$, the wake recovery increments were the highest for prescribed motions exclusively with cross-stream components (sway and roll). The cases with both cross-stream and streamwise components (pitch and yaw) showed intermediate wake recovery increments, while the case with a streamwise component exclusively (surge) showed the lowest wake recovery increments. These results suggest higher wake recovery benefits for cross-stream prescribed motions, as also reported by Fontanella et al. (2024, 2025) and Messmer et al. (2025). Messmer et al. (2025) linked this to higher increases in the Reynolds shear stress gradients in sway, especially in the streamwise-lateral direction, when compared to surge. In terms of the earlier onset of the wake recovery identified for SwHS and RoHS, Messmer et al. (2024) also show that the prescribed motion accelerates the wake recovery by shifting the position where the recovery gradient increases sharply. Since the SwHS and RoHS cases show the highest values of wake recovery, this could explain the observation of the earlier onset of the wake recovery for these cases in Fig. 6 (a).

The wake recovery gradient increments of the high-St_p/low-A^*_p cases are plotted in Fig. 6 (c) and highlight a notable trend. With the exception of the SuHS case, the wake recovery accelerates relative to that of the fixed-bottom case between $x^* = 1$ and $x^* = 3$, decelerates notably approaching levels close to the fixed-bottom case at $x^* = 4$, and accelerates again from $x^* = 5$ onward. These sharp variations in wake recovery gradient increments contrast with the relatively smooth variations observed in the low-St_p/high-A^*_p cases in Fig. 6 (b). These trends are linked to the wake morphology in Section 3.4.

The hampered recovery of the SuHS case observed in Fig. 6 (b) may be explained by differences in wake morphology that arise from the different motion excitations. The wake morphology is analyzed in vertical longitudinal slices of instantaneous streamwise velocity magnitude U_x/U_0 crossing the wake center in Fig. 7. This is done for the fixed-bottom (a), SuHS (b) and SwHS (c) cases. First, unlike the SwHS case, the SuHS case did not lead to noticeable meandering of the inner jet emanating from the rotor center, between $x^* = 2$ and $x^* = 4$, which is the region where the SwHS case experiences strong wake recovery. Second, the pulsating structures created by the SuHS motion appear to lead to larger dark blue areas than both the fixed-bottom and SwHS cases, which are regions of lower streamwise velocity. The higher benefits to wake recovery from the meandering structures induced by sway motions, when compared to the pulsating structures induced by surge motions are well-documented by Messmer et al. (2025). While Messmer et al. (2024, 2025) did not observe a deterioration of wake recovery in surge compared to the fixed-bottom case, Li et al. (2022) observed this deterioration for a sway case at $St_\mathrm{p} = 0.8$ and $A^*_\mathrm{p} = 0.04$ between $x^* = 6$ and $x^* = 8$. This supports the idea that there may be combinations of St_p and A^*_p that hamper wake recovery, similarly to what happens in the SuHS case in this study.

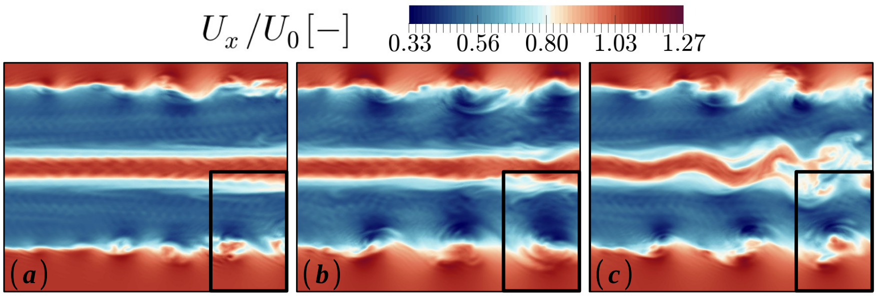

Figure 7. Instantaneous streamwise velocity at vertical longitudinal slices crossing the wake center for the fixed-bottom (a), SuHS (b) and SwHS (c) cases. The slices were taken between $x^* = 2$ and $x^* = 4$, at $t = 64$ s, which is the last instant of the simulations. The black rectangle highlights differences in the velocity field induced by the wake structures.

3.2 Turbulence intensity

This section investigates the effect that the prescribed motion has on the wake turbulence intensity and its connection to the wake recovery. To this end, the unidirectional turbulence intensity I_i was used:

$$I_i = \frac{< U_i'^2 >^{1/2}}{<|U|>}, \tag{9}$$

where $U_i' = U_i - <U_i>$, $i \in \{x, y, z\}$ and $|\cdot|$ denotes the vector norm. The evolution of the streamwise turbulence intensity I_x can be seen in Fig. 8 for several cases. The black region on the top of each contour corresponds to the upper wall. Each row represents one downstream position while each column represents one case. The smooth plots were obtained via linear interpolation.

All floating cases show higher values of I_x compared to the fixed-bottom case at $x^* = 2$ and $x^* = 4$, indicating that the prescribed motion is driving turbulence production in the wake. At $x^* = 4$, there is a clear increase in I_x at the wake center for the floating cases, a phenomenon that was also observed by Fontanella et al. (2024). The surge cases lead mostly to increases in I_x within the rotor perimeter, while the sway cases lead to a broader increase in I_x, especially at the rotor perimeter and outside, as observed in Messmer et al. (2025). The pitch case also leads to a broader increase in I_x. The spatial dispersion of I_x tends to follow the prescribed motion at $x^* = 2$ (e.g., higher cross-stream dispersion for sway), suggesting that the wake is retaining the geometrical features of the prescribed motion at this location. Similarly to Fig. 5, Fig. 8 supports the observation of stronger wake destabilization in the high-St_p/low-A_p^* cases compared to the fixed-bottom and the low-St_p/high-A_p^* cases, indicated by the higher dispersion of I_x at $x^* = 4$ and more irregular edges at $x^* = 4$ and $x^* = 6$ for the SwHS and PiHS cases. The profiles of the remaining high-St_p/low-A_p^* cases, except the SuHS case, are similar to those of the SwHS and PiHS cases. This destabilization is now more clearly observed both at the outer boundary of the wake, as well as in its core. The exception is once again the SuHS case, whose I_x profile retained a regular circular shape like the fixed-bottom and the low-St_p/high-A_p^* cases. The I_x profiles of the remaining low-St_p/high-A_p^* cases are very similar to those of the SwLS case, and are characterized by a regular circular shape with higher values of I_x at the rotor perimeter and the wake core, when compared to the fixed-bottom case.

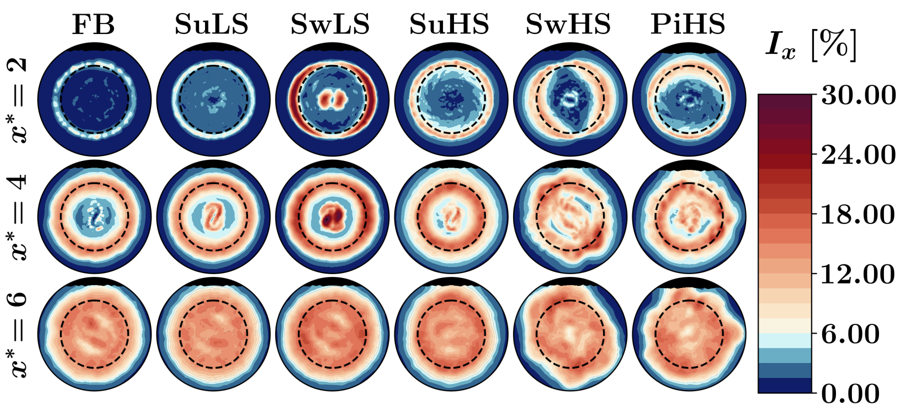

Figure 8. Streamwise turbulence intensity over the radial probes at several downstream positions. The black region corresponds to the upper wall. The black dashed circle delimits the rotor perimeter

Following the same process of the previous section, the values of turbulence intensity were spatially averaged to allow for an easier comparison between cases. Figure 9 (a) shows the spatially averaged values of both the streamwise ($\overline{I_x}$) and cross-stream ($\overline{I_y}$) turbulence intensities for the fixed-bottom case. Both turbulence intensities display a sharp increase between $x^* = 1$ and $x^* = 6$, and drop at $x^* = 7$. The values of $\overline{I_x}$ are slightly higher than the values of $\overline{I_y}$ from $x^* = 3$ onward.

Figures 9 (b) and (c) show the streamwise and cross-stream turbulence intensity increments, respectively. The turbulence intensity increments represent the difference in turbulence intensity relative to the fixed-bottom case, in analogy to Equation 7. These increments are absolute differences between physical quantities measured in percentage, and hence are also measured in percentage. The high-St_p/low-A^*_p cases show markedly higher $\overline{I_x}$ increments than the low-St_p/high-A^*_p cases between $x^* = 2$ and $x^* = 4$, and vice-versa after $x^* = 5$. For $\overline{I_y}$, the high-St_p/low-A^*_p cases show higher increments than the low-St_p/high-A^*_p from $x^* = 2$ to $x^* = 5$, and the difference is notably larger than it was for $\overline{I_x}$. Indeed, while the $\overline{I_x}$ and $\overline{I_y}$ increments of the high-St_p/low-A^*_p cases were of the same order, the $\overline{I_y}$ increments of the low-St_p/high-A^*_p cases were lower than the $\overline{I_x}$ increments. Both the $\overline{I_x}$ and $\overline{I_y}$ increments of the high-St_p/low-A^*_p cases increase sharply, peaking between $x^* = 3$ and $x^* = 4$, and decrease sharply afterwards. In contrast, the low-St_p/high-A^*_p increments either increase slowly or do not increase at all until $x^* = 5$, before dropping. Li et al. (2022) also observed sharp increases and decreases in turbulence intensity between $x^* = 2$ and $x^* = 6$, where the magnitude of the increases and decreases was largest for $St = 0.3$ and decreased for other Strouhal numbers. Higher values of turbulence intensity were associated with a faster wake recovery in Li et al. (2022), similarly to what is overall observed in this study when comparing the high-St_p/low-A^*_p cases to the low-St_p/high-A^*_p cases (see Fig. 6 and Fig. 9). The exception was the SuHS, whose pulsating structures likely increased turbulence intensity but decreased the velocity in the wake, as observed in Fig. 7.

Within the high-St_p/low-A^*_p cases, the $\overline{I_x}$ increments are relatively close. On the other hand, between $x^* = 3$ and $x^* = 4$, the $\overline{I_y}$ increments were the highest for prescribed motions exclusively with cross-stream components (sway and roll). The cases with both cross-stream and streamwise components (pitch and yaw) showed intermediate $\overline{I_y}$ increments. The case with a streamwise component exclusively (surge) showed intermediate levels at $x^* = 3$ and the lowest levels at $x^* = 4$. The wake recovery values were ordered broadly in the same way as the cross-stream turbulence intensity values for these cases at the same locations (see Fig. 6 (b)), suggesting that the cross-stream turbulence intensity has a more important role in driving the wake recovery than the streamwise turbulence intensity. The cross-stream turbulence intensity is very likely a reflection of stronger cross-stream meandering structures, which were found to be more effective in promoting wake recovery by Messmer et al. (2025). Additionally, Messmer et al. (2024) reported that sway motions generate more turbulence overall than surge motions, as observed in this study.

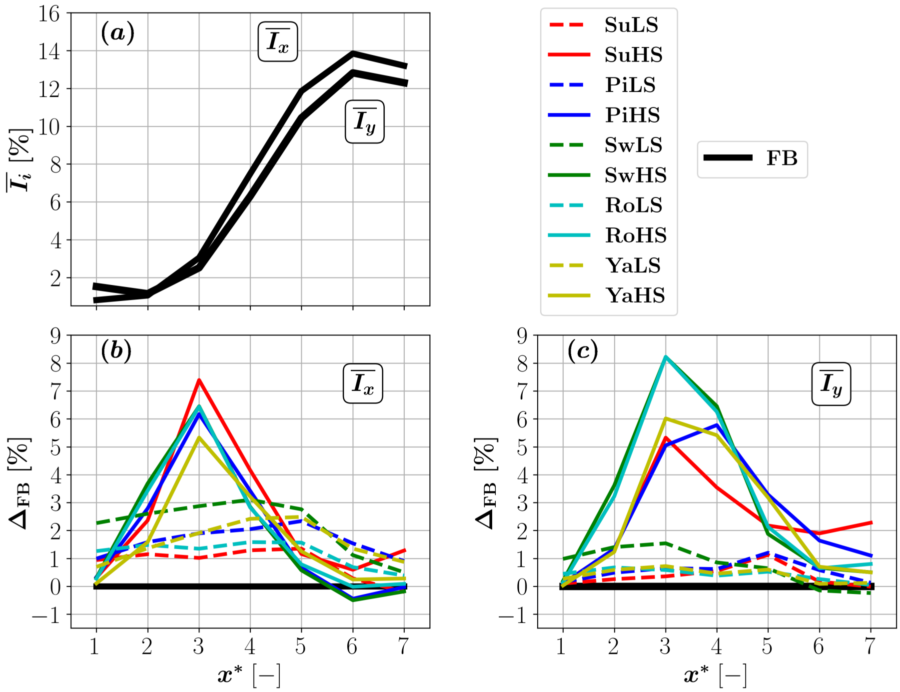

Figure 9. Evolution of the spatially averaged streamwise and cross-stream turbulence intensities for the fixed-bottom case (a), streamwise turbulence intensity increments (b), and cross-stream turbulence intensity increments (c). The turbulence intensity increments are absolute differences relative to the fixed-bottom case. The fixed-bottom case is shown in black, the high-St_p/low-A^*_p cases are shown in solid lines, and the low-St_p/high-A^*_p cases are shown in dashed lines.

3.3 Frequency contents

So far, different wake recovery and turbulence intensity trends were identified for different Strouhal numbers and prescribed motion directions, that are in agreement with the literature. This section identifies the effect that different prescribed motions have on the wake spectrum, how much the prescribed motion is amplified by the wake, and which regions of the wake amplify the perturbation introduced by the prescribed motion.

The spectrum at a given point in the wake was defined by the power spectrum of the cross-stream velocity component:

$$\frac{P_{yy}(St)}{{U_0}^2} = \frac{|\widehat{U_y}(t)|^2}{{U_0}^2}, \tag{10}$$

where $\widehat{\cdot}$ denotes the fast Fourier transform (FFT) and $|\cdot|$ denotes the complex number modulus. The cross-stream component was used specifically because prior results and the literature suggest that cross-stream meandering structures are the most important for driving the wake recovery. The wake spectra were computed for each point in each radial probe. Then the wake spectra were spatially averaged within the rotor perimeter with a simple ensemble average, resulting in the average wake spectrum $\overline{P_{yy}}(St)/U_0^2$ for each downstream position.

Figure 10 shows the evolution of the average wake spectrum for the fixed-bottom and both sway cases. The red lines are the first three multiples of the rotational Strouhal number St_r. The blue lines are the first three multiples of the prescribed motion Strouhal number St_p. The green lines are the sum and difference between the 3P Strouhal number ($3St_\mathrm{r} = 7.14$) and St_p. The plot indicates that the fixed-bottom case developed velocity perturbations that concentrated in the range of approximately $0.5 \leq St \leq 1.5$ at $x^* = 4$. At $x^* = 6$, the range narrows to $0.5 \leq St \leq 1$ with a peak at $St = 0.5$. The range where the velocity perturbations are concentrated at $x^* = 4$ and the peak St at $x^* = 6$ overlap with the most favorable range for upstream perturbation amplification found in the literature ($0.1 \leq St \leq 0.9$). The slope at high frequencies approached minus five-thirds, as expected for freely decaying turbulence at high Re.

The sway cases show peaks at St_p, St_r and their multiples. Moreover, there were peaks equal to the sums and differences between St_r and St_p, and between their multiples, indicating some interaction between the prescribed motion frequency and the rotational frequency that vanishes as the wake progresses downstream. This led to multiple peaks concentrated around the 3P Strouhal number at $x^* = 2$ and $x^* = 4$. For both sway cases, the prescribed motion Strouhal number was amplified between $x^* = 2$ and $x^* = 4$ and decayed afterwards. At $x^* = 6$, it is still possible to observe a peak at the prescribed motion Strouhal number that is much stronger for the SwHS case. Although not included in this manuscript, the spectra of the remaining high-St_p/low-A_p^* cases and low-St_p/high-A_p^* cases were very similar to the spectra of SwHS and SwLS, respectively.

The spectra suggest an explanation as to why the high-St_p/low-A_p^* cases present stronger wake perturbations than the low-St_p/high-A_p^* cases, despite the corresponding prescribed motion Strouhal number ($St_\mathrm{p} = 1.1905$) being outside the most favorable range in the literature. Contrary to the low-St_p/high-A_p^* cases ($St_\mathrm{p} = 0.0744$), the prescribed Strouhal number in the high-St_p/low-A_p^* cases was within the range at which the wake developed velocity perturbations in the fixed-bottom case at $x^* = 4$, i.e., $0.5 \leq St \leq 1.5$. This range should represent the natural modes of the wake and exciting those modes should lead to their amplification. The outcome of this would be higher values of the prescribed motion spectral components for the

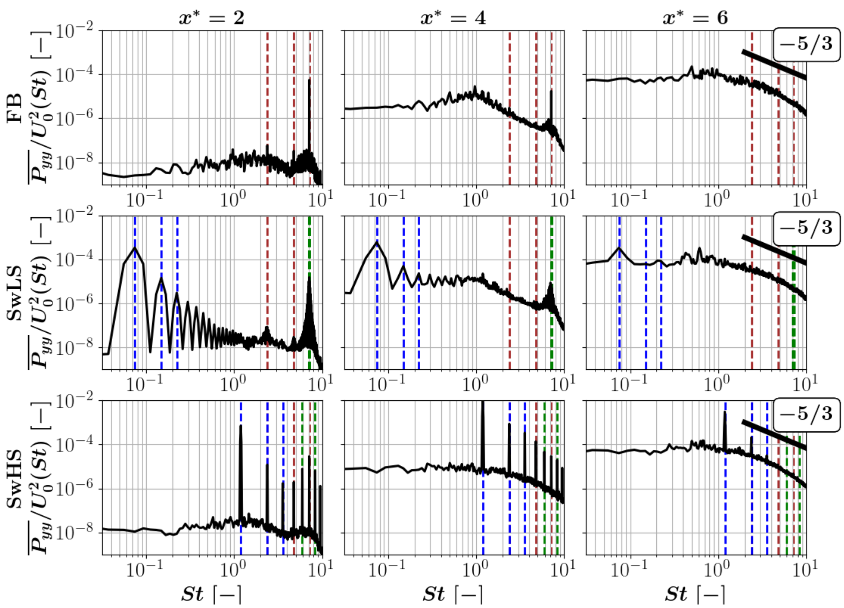

Figure 10. Average wake spectra of the cross-stream velocity component. The red lines are the first three multiples of the rotational Strouhal number St_{r}. The blue lines are the first three multiples of the prescribed motion Strouhal number St_{p}. The green lines are the sum and difference between the 3P Strouhal number ($3St_{\mathrm{r}} = 7.14$) and St_{p}.

high-St_{p}/low-A_{p}^* cases, which was indeed what was found. Fontanella et al. (2024) performed experimental surge and pitch cases at approximately the same Strouhal number as the high-St_{p}/low-A_{p}^* cases in this study, and observed wake oscillations at that Strouhal number at the boundaries of the wake. This supports the observation of wake excitation at $St_{\mathrm{p}} = 1.1905$ in this study, despite the fact that it was outside of the most favorable range found in the literature.

The amplification of the different prescribed motions in the wake is now quantified below, using the FFT amplitude method of Li et al. (2022) extended to a two-dimensional wake section. First, the dimensional cross-stream velocity amplitude spectrum $A_y(St)$ was computed at each point in each radial probe. Second, the spectral component at the prescribed motion frequency $A_y(St_{\mathrm{p}})$ was extracted for every point. Third, this component was spatially averaged within the region bounded by the rotor perimeter at each radial probe, and normalized, resulting in the average cross-stream velocity spectrum at the prescribed motion frequency (see Equation 6 for the spatial averaging process):

$$\frac{\overline{A_y}(St_{\mathrm{p}})}{U_0} = \left.\frac{\overline{|\widehat{U_y}(t)|}}{U_0}\right|_{St=St_{\mathrm{p}}}, \tag{11}$$

where $\widehat{\cdot}$ denotes the fast Fourier transform (FFT), $|\cdot|$ denotes the complex number modulus and $\overline{}$ denotes the spatial average. From this, the cross-stream velocity amplification factors (called FFT amplitudes in Li et al. (2022)) were computed:

$$k_y(St_{\mathrm{p}}) = \frac{\overline{A_y}(St_{\mathrm{p}})/U_0}{A_{\mathrm{prc}}\omega_{\mathrm{p}}/U_0} = \frac{\overline{A_y}(St_{\mathrm{p}})}{A_{\mathrm{prc}}\omega_{\mathrm{p}}}, \tag{12}$$

where A_{prc} is the dimensional prescribed motion amplitude at the rotor center and ω_{p} is the dimensional prescribed motion angular frequency. $A_{\mathrm{prc}}\omega_{\mathrm{p}}$ represents the dimensional prescribed motion velocity amplitude at the rotor center. For yaw, $A_{\mathrm{prc}}\omega_{\mathrm{p}}$ represents the dimensional prescribed motion velocity amplitude at the tip of a blade with an azimuth of $\theta = 90$ deg. The amplification factors assess the cross-stream velocity perturbations in the wake against the initial prescribed motion velocity perturbation. This was done because some prescribed motions might have had a stronger presence in the wake simply because the initial perturbation was stronger.

Figure 11 shows the amplification factors for all floating cases. All the high-St_{p}/low-A_{p}^* cases showed a sharp amplification of cross-stream velocity perturbations, that peaked between $x^* = 3$ and $x^* = 5$, and dropped afterwards. This was broadly the same region where a sharp increase in cross-stream turbulence intensity was observed in Fig. 9, suggesting a strong relationship between the prescribed motion and the wake perturbation. Li et al. (2022) observed the same sharp increase and decrease in FFT amplitude at the prescribed motion frequency for sway at $0.2 \leq St_{\mathrm{p}} \leq 0.6$. Messmer et al. (2024) defined the amplification factors in terms of the ratio of the energy of the most energetic coherent structures to the prescribed motion energy, and observed the same pattern of sharp increase and decrease for the amplification factors in surge, but most notably for $St_{\mathrm{p}} \leq 0.38$. In contrast with the high-St_{p}/low-A_{p}^* cases, the low-St_{p}/high-A_{p}^* cases showed a much weaker amplification overall, which could be due to the fact that the prescribed motion Strouhal number was outside the most favorable range identified in the literature and in the fixed-bottom case spectrum. The higher amplitude of these cases may have also played a role, following the observation by Messmer et al. (2024, 2025) that, for the same Strouhal number, prescribed motions with higher amplitudes have a smaller amplification potential relative to the initial perturbation.

Within the high-St_{p}/low-A_{p}^* cases, the amplification was strongest for the cases with a cross-stream component (yaw, roll, sway and pitch), and weakest for the case with a streamwise component only (surge). This comes as expected since the amplification factors refer to the cross-stream velocity perturbations.

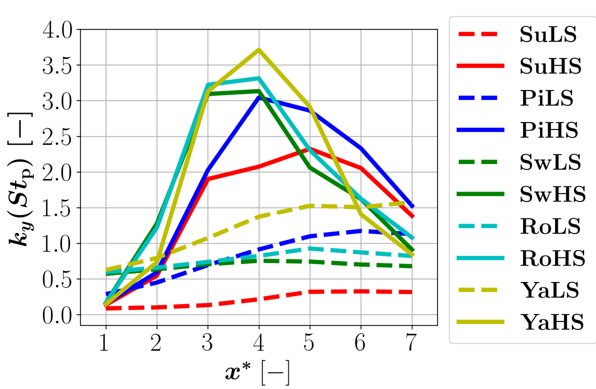

Figure 11. Cross-stream velocity amplification factors at the prescribed motion frequency. There is no curve for the fixed-bottom case because there was no prescribed motion.

The average cross-stream velocity spectrum and cross-stream velocity amplification factors provide information about how each section of the wake reacted globally to the prescribed motion, but these quantities do not provide information about the local behavior. For this, one can observe the cross-stream velocity spectrum $A_y(St_\mathrm{p})/U_0$, i.e., prior to the spatial averaging, at each section of the wake.

Figure 12 shows the cross-stream velocity spectrum at the prescribed motion frequency. The black region on the top of each contour corresponds to the upper wall. Each row represents one downstream position while each column represents one case. The smooth plots were obtained via linear interpolation. The white dashed circle indicates the rotor perimeter. For the fixed-bottom, SuLS and SwLS cases, there was virtually no excitation of the wake. On the other hand, the wakes of the SuHS, SwHS and PiHS cases were much more excited, particularly immediately outside the rotor perimeter and at the rotor center. As previously mentioned, Fontanella et al. (2024) experimentally observed this excitation at the prescribed motion frequency at the wake boundaries for surge and pitch cases at approximately the same Strouhal number as the high-St_p/low-A_p^* cases. This naturally points towards the tip and root vortices and the associated shear layers as the amplification regions, as expected due to their strong amplification potential (Gupta and Wan, 2019; Messmer et al., 2025). Hence, these regions are analyzed in detail in the following section.

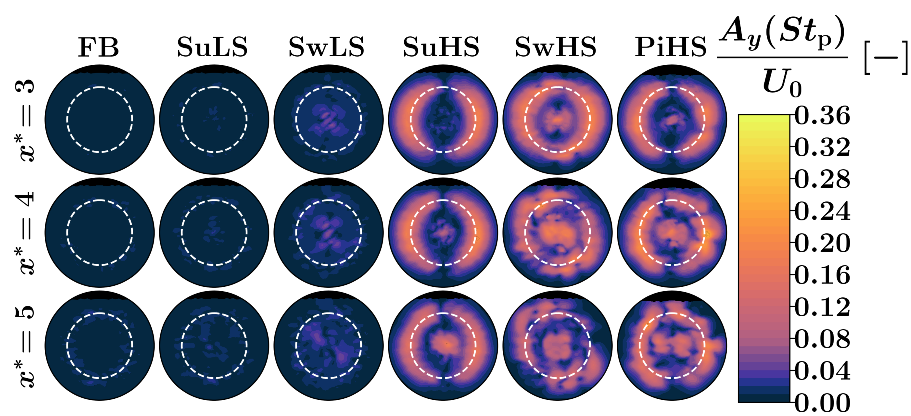

Figure 12. Cross-stream velocity spectrum at the prescribed motion frequency over the radial probes at several downstream positions. The black region corresponds to the upper wall. The white dashed circle indicates the rotor perimeter.

3.4 Tip and root vortex trails

The tip vortices can be visualized by plotting the Q-criterion QD^2/U_0^2 that indicates regions where the local rotation rate is larger than the local strain rate. Figure 13 shows the surface $QD^2/U_0^2 = 2.48$ for the fixed-bottom (a), SuLS (b), SuHS (c), SwHS (d) and YaHS (e) cases, respectively. The SuLS case showed virtually no difference in the evolution of the tip vortices compared to the fixed-bottom case. The SuHS case, on the other hand, showed a pulsating tip vortex, which was likely caused by the earlier onset of the leap-frogging phenomenon, and followed by the merging between two consecutive tip vortices. These coherent structures were more pronounced and dissipated less as the wake progressed downstream than in the fixed-bottom and SuLS cases. The SwHS case showed a diagonally deformed tip vortex envelope, indicating lateral meandering (i.e., movement in the y^* direction), consistent with the sway motion direction. The coherent structures appear to dissipate earlier in this case, when compared with the SuHS case, suggesting a faster transition to the far-wake. Both the pulsating and meandering coherent structures observed in the SuHS and SwHS cases, respectively, have been documented in the literature, as a response to upstream flow perturbations (Li et al., 2022; Fontanella et al., 2024; Messmer et al., 2024, 2025). The yaw motion was found to induce coherent structures similar to those of the sway motion, with lateral meandering as well, which was also observed by Fontanella et al. (2024).

The tip and root vortices were further analyzed to evaluate wake morphology differences between cases, namely the thickness of the tip and root vortex trails and the downstream position where they merge. Before moving on, it is important to reflect on the effect that these vortices have on the flow field and to define exactly what "trail" means, in the context of this analysis. A viscous vortex is a flow structure that induces tangential velocity in the flow. Taking the Lamb-Oseen model as an example, the tangential velocity is zero at the vortex core, increases up to a certain distance from the core, and then decays to zero farther away from the core. In other words, a vortex is a structure that introduces large velocity gradients in the flow, and its convection in the wake causes a high degree of variability in both the magnitude and direction of the velocity field in time. Based on this, the vortex trails were defined as the regions in the wake that show a degree of velocity field magnitude variability in time above a certain threshold. The metric used to measure velocity field magnitude variability was the standard deviation of the magnitude of the velocity field $<|U|'^2>^{1/2}/U_0$ after convergence (i.e., for $t \geq 32$ s).

The analysis of the tip and root vortex trails and the parameter $<|U|'^2>^{1/2}/U_0$ was done at longitudinal domain slices perpendicular to the height of the domain and crossing the rotor center, i.e., defined by the plane $z^* = z^*_{\mathrm{rc}} = z^*_{\mathrm{p}} + L_1$ in Fig. 1 (b), where z^*_{rc} is the rotor center height. Figure 14 shows $<|U|'^2>^{1/2}/U_0$ for the SwLS (a) and SwHS (b) cases, respectively. Both cases are sway cases, which means that the turbine was oscillating in the cross-stream direction (y^*). These cases show two regions of high $<|U|'^2>^{1/2}/U_0$ that emanate from the blade tips and roots, and correspond to the tip and root vortex trails. In order to quantify the trail thickness, the trails were delimited in these planes by choosing a value of $<|U|'^2>^{1/2}/U_0$ that would closely contain the region of high $<|U|'^2>^{1/2}/U_0$ in the SwLS case. The chosen value was $<|U|'^2>^{1/2}/U_0 = 0.044$ and the trail limits arising therefrom are plotted as a yellow line in Fig. 14. The same value was used to track the trail limits of all cases in order to make them comparable. It can be seen that the tip and root vortex trail regions from both cases differ. In the SwLS case, the tip trail thickness remains approximately constant up to $x^* \approx 2$ and then starts increasing. The root trail thickness remains almost unchanged. In the SwHS case, the tip trail thickness is much lower than in the SwLS case before $x^* \approx 1.5$, but increases abruptly at that position. Then, it decreases at $x^* \approx 3$, and increases again further downstream, leading to a bulb-shaped contour. The root trail thickness decreases sharply until $x^* \approx 2$ and then increases sharply from that point.

Figure 15 (a) shows the tip vortex trail limits from Fig. 14 (i.e., from the SwLS and SwHS cases) and from the fixed-bottom case in the region defined by $y^* > y^*_{\mathrm{rc}}$, where y^*_{rc} is the y^* coordinate of the rotor center. The red horizontal line indicates the tip position which is $y^* = 0.5$. y^*_1 represents the limit that is closest to the free stream, while y^*_2 represents the limit that is closest to the wake center. Computing the total thickness of the trail (i.e., $y^*_1 - y^*_2$) would have led to discontinuities in the thickness growth rate because the tip and root trails merge at some point, making y^*_2 constant. This can be observed, for instance, in the

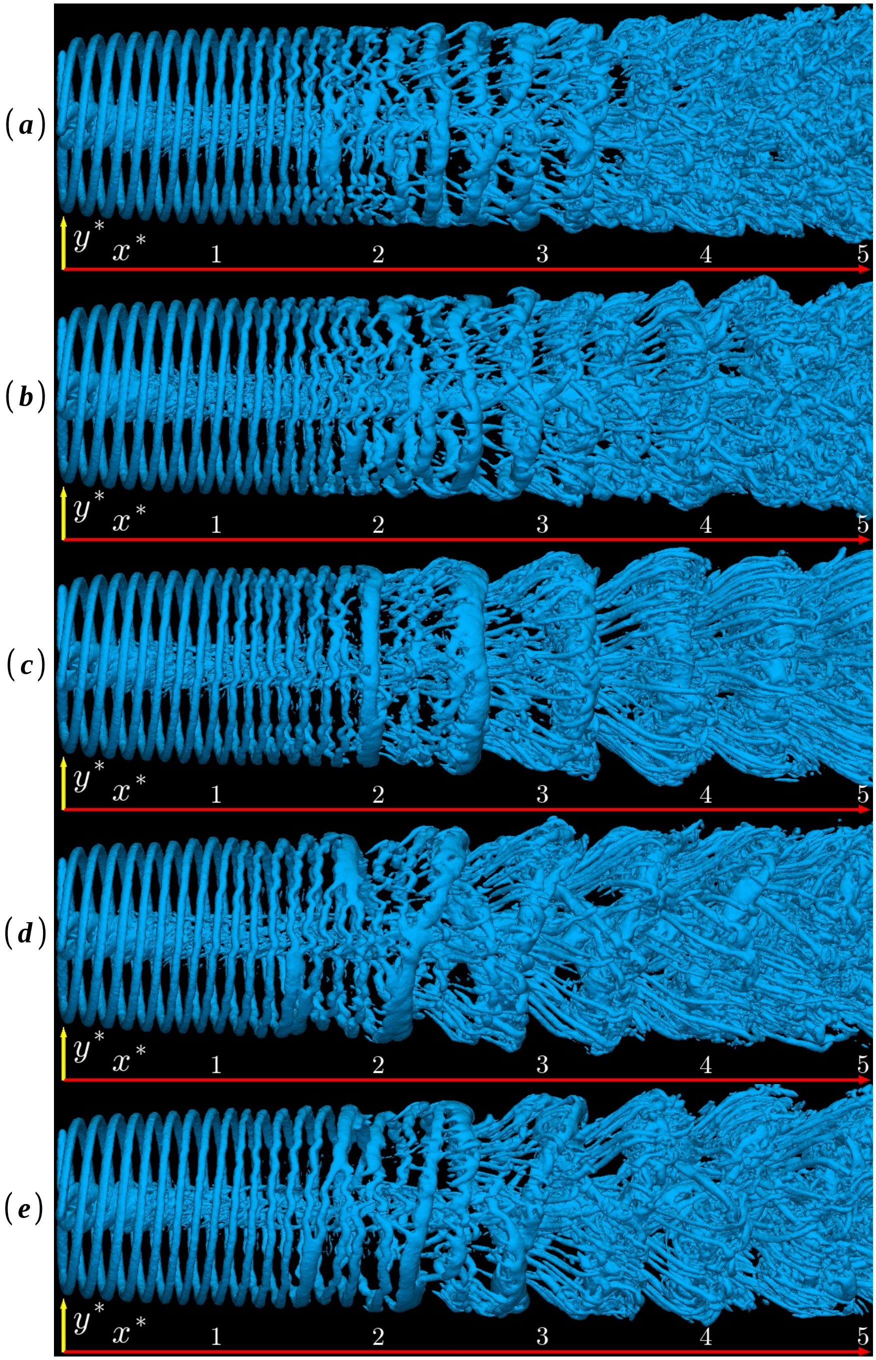

Figure 13. Q-criterion surface $QD^2/U_0^2 = 2.48$ for the fixed-bottom (a), SuLS (b), SuHS (c), SwHS (d) and YaHS (e) cases.

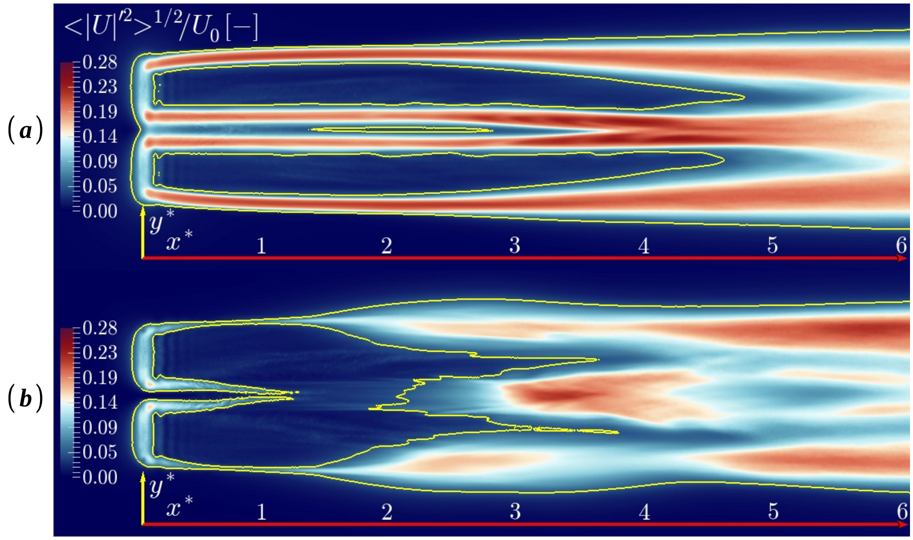

Figure 14. Standard deviation of the velocity magnitude for the SwLS case (a) and the SwHS case (b). The plane is a longitudinal domain slice perpendicular to the height of the domain and crossing the rotor center. The tip and root vortex trails are delimited by the yellow line, which is the region where $<|U|'^2>^{1/2}/U_0 = 0.044$.

SwLS case at $x^* \approx 4.7$ in Fig. 14 (a) and Fig. 15 (a). Instead, the trail half-thickness was defined as the difference between y_1^* and the tip position (i.e., $y_1^* - 0.5$), and was used to quantify the trail evolution.

Figure 15 (b) shows the tip vortex trail half-thickness for all the cases. It can be seen that the trail half-thickness of the low-St_p/high-A_p^* and fixed-bottom cases increases at an approximately constant rate. In comparison, the trail half-thickness of the high-St_p/low-A_p^* cases increases sharply from $x^* \approx 1$ to $x^* \approx 3$, decreases between $x^* \approx 3$ and $x^* \approx 5$, and increases again therefrom. The region of the sharp increase in the tip vortex trail half-thickness coincides with the regions where both the streamwise and cross-stream turbulence intensities also exhibit a sharp increase (see Fig. 9 (b) and (c)), indicating that the expansion of the wake and the increase in turbulence are happening simultaneously.

It is now shown that the expansion of the tip vortex trail happens simultaneously with the excitation of the trail at the prescribed motion frequency in the high-St_p/low-A_p^* cases. This was done by comparing the evolution of the total trail thickness ($y_1^* - y_2^*$) to the evolution of the average cross-stream velocity spectrum at the prescribed motion frequency $\overline{A_y}(St_\mathrm{p})/U_0$ along the thickness. The total trail thickness was used instead of the half-thickness, in spite of the discontinuity in the thickness growth rate, to capture the effect on the whole trail. The average cross-stream velocity spectrum metric is analogous to the one defined in Equation 11, but the spatial average was computed over the trail thickness only. Figure 16 shows the comparison of the total trail thickness and the average cross-stream velocity spectrum at the two tip vortex trails, for the SwLS case (left) and the SwHS case (right). Quantities in the $y^* > y_\mathrm{rc}^*$ region are shown in solid line, while quantities in the $y^* < y_\mathrm{rc}^*$ region are shown in dashed line. The total trail thickness is shown in red and the average cross-stream velocity spectrum is shown in magenta. For the SwLS case, it can be seen that the trail expansion was not accompanied by a large increase in $\overline{A_y}(St_\mathrm{p})/U_0$.

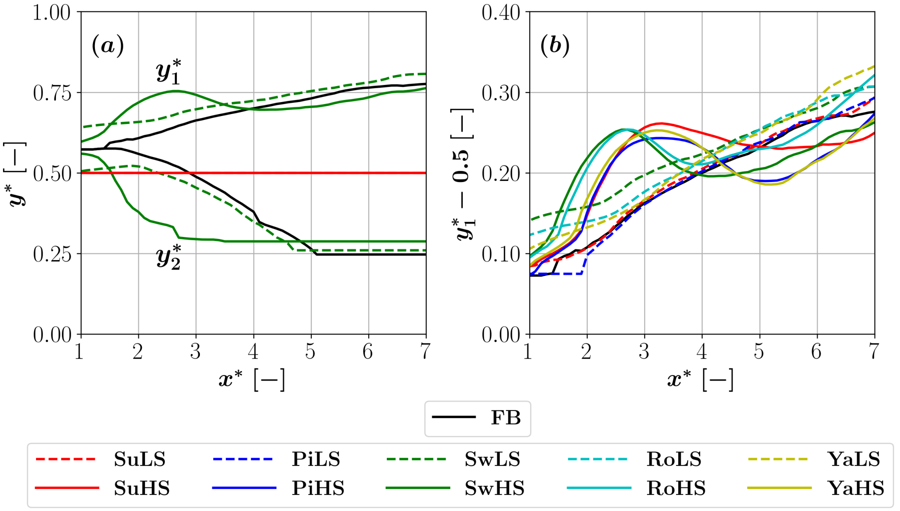

Figure 15. (a) Tip vortex trail limits at the $y^* > y^*_{\mathrm{rc}}$ region for the fixed-bottom, SwLS and SwHS cases. The red line indicates the tip position; (b) Tip vortex trail half-thickness for all cases.

Conversely, for the SwHS case, there was a sharp increase in $\overline{A_y}(St_{\mathrm{p}})/U_0$ that peaked at approximately the maximum thickness position, providing evidence that the early tip vortex trail expansion was triggered by the prescribed motion excitation. The same behavior found in the SwLS and SwHS cases was observed for the remaining low-St_{p}/high-A^*_{p} cases and high-St_{p}/low-A^*_{p} cases, respectively.

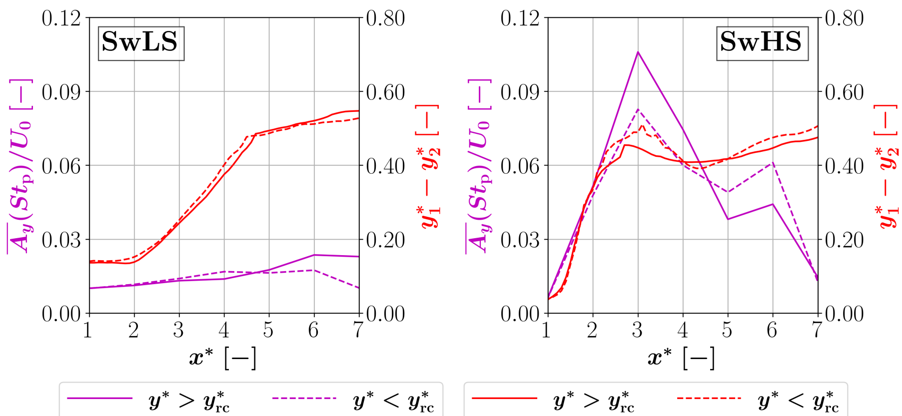

Figure 16. Total trail thickness (red) and average cross-stream velocity spectrum at the prescribed motion frequency (magenta) for the SwLS (left) and SwHS (right) cases in the plane of Fig. 14.

A necessary condition for the transition to the far-wake is the merger between the tip and root shear layers. Hence, an earlier merger should indicate an earlier transition to the far-wake, and a faster recovery as a consequence of the improved flow mixing.

With the goal of linking the wake recovery to the tip and root shear layer merger, the tip and root vortex trail limits defined above were used as a proxy for the merger between shear layers. The mergers between tip and root vortex trails were identified in the plane $z^* = z^*_{\mathrm{rc}}$ shown in Fig. 14, and in the plane $y^* = y^*_{\mathrm{rc}}$, which is a longitudinal plane orthogonal to the plane $z^* = z^*_{\mathrm{rc}}$. y^*_{rc} and z^*_{rc} are both rotor center coordinates. Each plane has two merger points associated with it, since there are two pairs of tip and root vortex trails. It is possible to observe some merger points in the plane $z^* = z^*_{\mathrm{rc}}$ shown in Fig. 14. The merger points of the SwLS case in Fig. 14 (a) are located close to $x^* \approx 4.7$. The merger points of the SwHS case in Fig. 14 (b) are located close to $x^* \approx 3.7$. The four merger points of all cases for both planes are compiled in Figure 17. The low-St_{p}/high-A^*_{p} cases show merger points that were very close to those of the fixed-bottom case, while the high-St_{p}/low-A^*_{p} cases clearly show merger points that are located more upstream. This finding is consistent with the overall faster wake recovery of the high-St_{p}/low-A^*_{p} cases, and showcases yet another difference between the low-St_{p}/high-A^*_{p} cases and the high-St_{p}/low-A^*_{p} cases. It is also noted that the merger points in the plane $y^* = y^*_{\mathrm{rc}}$ are almost always located more upstream than those in the plane $z^* = z^*_{\mathrm{rc}}$. This is probably caused by the domain asymmetry and proximity to the top wall, where the reduced height of the domain compared to its width may constrain the flow and cause earlier mergers. It is worth highlighting this phenomenon because it is likely to happen in asymmetric wind tunnels where the blockage ratio is high, such as the Politecnico di Milano wind tunnel that was reproduced in the simulations. In spite of this, there is a clear consistency in the results, in that the high-St_{p}/low-A^*_{p} cases show mergers earlier than the low-St_{p}/high-A^*_{p} cases in both planes.

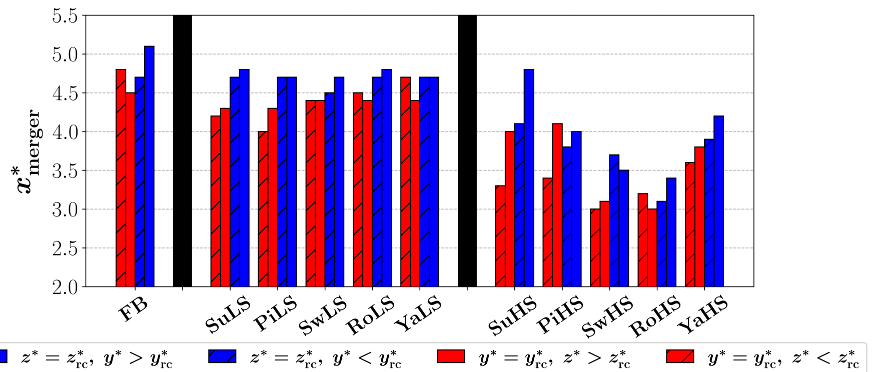

Figure 17. Tip and root trail merger points. The blue bars refer to the merger points in the plane $z^* = z^*_{\mathrm{rc}}$, which is the plane shown in Fig. 14. The red bars refer to the merger points in the plane $y^* = y^*_{\mathrm{rc}}$, which is a longitudinal plane orthogonal to the plane $z^* = z^*_{\mathrm{rc}}$. Bars with stripes correspond to positions below the rotor center. Bars without stripes refer to positions above the rotor center.

4 Discussion

The results of this study can be understood as a divide between two contrasting wake regimes, defined by the prescribed Strouhal number and amplitude. These were the low-St_{p}/high-A^*_{p} regime and the high-St_{p}/low-A^*_{p} regime, which produced consistently different wake behavior across all degrees of freedom and analyses performed. The origin of this divide can be traced to the frequency-selective amplification of upstream perturbations in the wake.

The low-St_{p}/high-A_{p}^* regime was characterized by a large upstream perturbation but low amplification in the wake. These cases produced a wake that was largely indistinguishable from the fixed-bottom case in terms of morphology, cross-stream turbulence intensity, and tip vortex trail evolution (see Figs. 13, 9 (c) and 15 (b)). This is somewhat counterintuitive, given that the prescribed motion amplitude in this regime was approximately ten times larger than that of the high-St_{p}/low-A_{p}^* regime. The explanation lies in the frequency content of the perturbation rather than its amplitude. The prescribed Strouhal number of these cases ($St_{\mathrm{p}} = 0.0744$) falls both below the most favorable range identified in the literature ($0.1 \leq St \leq 0.9$) and the frequency range in which the fixed-bottom wake naturally develops high spectral energy ($0.5 \leq St \leq 1.5$ at $x^* = 4$, see Fig. 10), meaning that the perturbation does not excite the natural modes of the wake. In the absence of resonance, the large-amplitude motion is not selectively amplified, and the velocity amplification factors remain low throughout the wake. This in turn leads to lower wake recovery increments and a gradual tip vortex trail expansion. The large amplitude of this regime might have also hindered the amplification of perturbations in the wake, according to Messmer et al. (2024, 2025), who noted that larger amplitudes produce a smaller amplification relative to the initial perturbation.

The high-St_{p}/low-A_{p}^* regime was characterized by a small upstream perturbation but high amplification in the wake. These cases, despite their much smaller prescribed amplitudes, produced a qualitatively different and more dynamic wake (see Figs. 5, 8 and 13). For these cases, the prescribed Strouhal number ($St_{\mathrm{p}} = 1.1905$), while outside the most favorable range identified in the literature, falls within the high-energy spectral region that the fixed-bottom wake develops naturally in the near wake. This suggests a resonance-like mechanism where, by exciting the wake at a frequency close to one of its natural modes, even a small perturbation can be amplified as it convects downstream. The experimental observations of Fontanella et al. (2024), who detected wake oscillations at the prescribed motion frequency specifically at the wake boundaries for cases at approximately the same Strouhal number, further support this. This amplification manifested as sharp peaks in the cross-stream velocity amplification factors between $x^* = 3$ and $x^* = 5$ (see Fig. 11), a pattern that is broadly consistent with Li et al. (2022) and Messmer et al. (2024), who observed the same sharp increase and decrease in amplification factors for sway and for surge, respectively. The amplified perturbations in the high-St_{p}/low-A_{p}^* regime were not distributed uniformly across the wake cross-section but were concentrated at the rotor perimeter and the rotor center (see Fig. 12), where the tip and root vortices and their associated shear layers are located. This was to be expected due to the amplification potential of shear flow instabilities under low turbulence and strong shear (Gupta and Wan, 2019; Messmer et al., 2025). The evidence for this in the present study is the bulb-shaped tip vortex trail expansion observed for the high-St_{p}/low-A_{p}^* cases (see Figs. 14 (b) and 15 (b)), where the steep early expansion of the trail was shown to coincide spatially with the peak of the prescribed motion spectral component along the trail (see Fig. 16 (right)). This coupling between prescribed motion excitation and tip vortex trail expansion, absent in the low-St_{p}/high-A_{p}^* regime, was the probable cause of the earlier mergers between the tip and root vortex trails (see Figs. 14 and 17), and was likely associated with the faster wake recovery (Messmer et al., 2024). The simultaneous sharp increases in streamwise turbulence intensity, cross-stream turbulence intensity, and wake recovery gradient (see Figs. 9 (b) and (c), and Fig. 6 (c)) in the same regions as the tip vortex trail expansion (see Fig. 15 (b)) further reinforce this picture, suggesting that the destabilization of the vortex trail, the increase in turbulence, and the acceleration of wake recovery are all manifestations of the same amplification process, consistent with the findings in the literature.

The SuHS case is a notable outlier within the high-St_p/low-A^*_p regime. Unlike the other cases in this group, the wake recovery was hampered between $x^* = 4$ and $x^* = 7$ relative to the fixed-bottom case (see Fig. 6 (b)), despite the high turbulence intensity produced in the wake (see Figs. 9 (b) and (c)). This can be attributed to the extreme simulated Strouhal number and the streamwise coherent pulsation structures that the simulated surge motion created (see Figs. 7 (b) and 13 (c)). The pulsating structures of the SuHS case were associated with virtually no inner jet meandering compared to the SwHS case, and larger low-velocity regions in the wake compared to both the fixed-bottom and SwHS cases. This exception underscores that the resonance mechanism alone is insufficient to guarantee beneficial wake recovery. Similarly, Li et al. (2022) observed detrimental effects on the wake recovery of a sway case at $St_\mathrm{p} = 0.8$ and $A^*_\mathrm{p} = 0.04$. The SuHS case in this study may represent an instance where this threshold has been crossed for surge cases.

In the high-St_p/low-A^*_p regime, prescribed motions with larger cross-stream components produced stronger wake recovery, higher cross-stream turbulence intensity, and higher cross-stream velocity amplification factors than prescribed motions with smaller cross-stream components (see Figs. 6 (b), 9 (c) and 11). The ordering of wake recovery increments among the high-St_p/low-A^*_p cases, with sway and roll highest, pitch and yaw intermediate, and surge lowest, mirrored the ordering of cross-stream turbulence intensity increments, suggesting that the cross-stream component of the motion is the quantity most directly responsible for the recovery benefit. These findings align with the experimental results of Fontanella et al. (2024, 2025) and Messmer et al. (2025), who identified cross-stream motions as the most beneficial for wake recovery. This is also reflected in the Q-criterion visualizations (see Fig. 13), which showed laterally meandering structures for sway and yaw, but pulsating structures for surge. Cross-stream perturbations excite meandering structures that have been identified as stronger drivers of wake momentum recovery, when compared to pulsating structures induced by streamwise perturbations, because they generate higher Reynolds shear stress gradients, particularly in the streamwise-lateral direction (Messmer et al., 2025).

The simulations were performed with sinusoidal motions under a laminar, uniform inflow and constant rotor speed. These simplifications, while useful to isolate the effects of the prescribed motion and aligned with the goals of the IEA task OC6 Phase III, have important implications for the interpretation of the results in the context of more realistic conditions. Turbulence in the inflow is known to both accelerate the wake transition, contributing as much as or more than the prescribed motion itself, and dissipate the coherent structures generated by the floating motion (Li et al., 2022; Pagamonci et al., 2025; Mian et al., 2025; Messmer et al., 2025; Firpo et al., 2026). Moreover, in realistic stochastic sea states that lead to platform motions across multiple degrees of freedom, Fontanella et al. (2025) reported that there may be no appreciable benefit to wake recovery. Both of these considerations suggest that selective amplification of upstream perturbations is likely to be less frequent under realistic conditions, and to be restricted to a narrower range of operating conditions characterized by low turbulence and steady wind. Additionally, the high blockage ratio of the setup (approximately 8.46%), the cross-section asymmetry, and the proximity of the rotor to the top wall likely introduced confinement effects, reflected in lower wake recovery (Fontanella et al., 2024) and earlier tip and root vortex mergers in the vertical plane (see the vertical plane in red and the horizontal plane in blue in Fig. 17), that are absent in full-scale offshore conditions. Despite these limitations, the phenomena identified in this study — frequency-dependent wake recovery, turbulence intensity increase, velocity perturbation amplification, pulsating and meandering coherent structures, tip vortex trail excitation and expansion, and earlier tip and root vortex mergers — are consistent with the results from full-scale simulations and less confined experimental setups found in the literature. These phenomena are expected to be enhanced for prescribed Strouhal numbers in the most favorable range identified in the literature ($0.1 \leq St \leq 0.9$).

5 Conclusions

This manuscript investigated the wake of a laboratory-scale floating offshore wind turbine under prescribed sinusoidal motions covering the surge, sway, roll, pitch, and yaw degrees of freedom, using large-eddy simulations coupled to an actuator-line model. The prescribed Strouhal numbers and amplitudes were chosen to be representative values of different FOWT support structures for surge and pitch, and the same values were applied to the remaining analogous degrees of freedom to enable a fair comparison. The simulation setup replicated the Politecnico di Milano wind tunnel cross-section, with the simultaneous goals of investigating the wake dynamics and assessing whether the results would be materially different under high-blockage-ratio conditions. The turbine was operated under constant rotor speed, near rated conditions, and steady, uniform inflow. This was done to isolate the effects of the prescribed motion on the wake evolution. Two cases per degree-of-freedom were considered, corresponding to two distinct wake regimes: one with a low Strouhal number and high amplitude, and one with a high Strouhal number and low amplitude.

The results highlighted clear differences between the two wake regimes. The low-St_p/high-A^*_p cases exhibited wake behavior that was largely indistinguishable from the fixed-bottom case, despite the prescribed amplitudes being approximately ten times larger than in the high-St_p/low-A^*_p cases. This was attributed to the prescribed Strouhal number falling both below the most favorable range identified in the literature and the frequency range in which the fixed-bottom wake naturally developed high spectral energy.

The high-St_p/low-A^*_p cases, by contrast, produced a more dynamic wake, characterized by more irregular wake boundaries, a faster wake recovery, stronger coherent structures, and faster tip and root vortex trail expansion. Contrary to the low-St_p/high-A^*_p cases, the prescribed Strouhal number fell within the high-energy spectral region naturally developed by the fixed-bottom wake, suggesting a resonance-like mechanism as the root cause of the differences. The resulting amplification of upstream perturbations was concentrated at the tip and root vortex trails and their associated shear layers, consistent with their known role as amplification regions due to shear flow instabilities. This excitation triggered a bulb-shaped expansion of the tip vortex trails, accompanied by sharp simultaneous increases in streamwise and cross-stream turbulence intensity. In turn, this led to earlier mergers between the tip and root vortex trails, a higher wake recovery gradient, and ultimately a faster wake recovery.

A notable outlier within the high-St_p/low-A^*_p cases was the surge case, which hampered the wake recovery, despite producing high turbulence intensity in the wake. This was attributed to the extreme simulated Strouhal number that led the pulsating coherent structures to produce larger low-velocity regions inside the wake, when compared to the fixed-bottom case and the high-St_p/low-A^*_p sway case.

Among the high-St_p/low-A_p^* cases, prescribed motions with larger cross-stream components produced stronger wake recovery, higher cross-stream turbulence intensity, and higher cross-stream velocity amplification factors, suggesting that the cross-stream component is most directly responsible for the recovery benefit, consistent with the observations in the literature.

Performing the simulations in this wind tunnel setup led to high-blockage-ratio conditions and likely caused wake confinement effects. The wake recovery values were lower than expected, likely due to a combination of extreme simulated Strouhal numbers and the inherent constraints of the wind tunnel setup. The asymmetry of the domain is thought to have produced earlier tip-root vortex trail mergers in the height direction compared with the lateral direction, a potential wind tunnel effect that is likely to occur in similar asymmetric setups. Despite these constraints, the conclusions are consistent with those found in the literature for less confined configurations, supporting the idea that the fundamental floating wind turbine wake dynamics identified in this study — frequency-dependent wake recovery, turbulence intensity increase, velocity perturbation amplification, pulsating and meandering coherent structures, tip vortex trail excitation and expansion, and earlier tip and root vortex mergers — are still captured under such confined conditions. These phenomena are expected to be enhanced for more favorable Strouhal numbers.

Appendix A: Blade kinematics validation

The prescribed motion implementation was validated against the theoretical solution of the motion of one point in one of the blades. Deriving the solution involved describing the rotor center coordinates as a function of the prescribed motion, and then summing the point motion relative to the rotor center due to rotation. Under prescribed translation, the variation in the value of the coordinates of all the turbine points due to the prescribed motion is exactly the same as the prescribed motion affecting those coordinates. Under prescribed rotation, the points on the turbine experience a variation in the value of the coordinates that is proportional to the distance to the rotation axis. Recalling the prescribed motion expression in Equation 2, the sign was negative for translation and positive for rotation, in accordance with the IEA task OC6 Phase III (Bergua et al., 2023). The coordinates in time for an arbitrary point in the blade on the reference frame $\boldsymbol{e_x}$-$\boldsymbol{e_y}$-$\boldsymbol{e_z}$ (see Fig. 1), with an initial azimuth of $\theta_0 = 0$ deg are shown in Table A1, where $\theta = \omega_\mathrm{r} t$ is the azimuth of a point in the blade; $\omega_\mathrm{r} = 2\pi f_\mathrm{r}$ is the rotor angular frequency; t is the time; R is the point's radial position relative to the rotor center; $L_\mathrm{e} = \sqrt{L_1^2 + L_2^2}$ is the distance from the rotor center to the pitch axis (where "e" stands for effective), and $\alpha_\mathrm{e} = \tan^{-1}(L_2/L_1)$ is the effective angle between the rotor center and the vertical direction. The rotor azimuth angle θ was defined as the azimuth of the blade that is upward pointing at the start of the simulation, i.e., the blade with $\theta_0 = 0$ deg.

The validation was performed by comparing the displacement calculated with the above expressions with the actual value from the simulations, by means of an error parameter. The displacement was defined as:

$$\frac{\Delta x_i}{L_\mathrm{b}} = \frac{x_i(t) - x_{i0}}{L_\mathrm{b}}, \tag{A1}$$

where i is the direction, L_b is the blade length, and x_{i0} is the initial value of the coordinate x_i. The displacement indicates how much the coordinate changed relative to the blade length. The relative error RE was defined as follows:

$$RE = \frac{\Delta x_i|_\mathrm{sim} - \Delta x_i|_\mathrm{theo}}{A_\mathrm{pp}}, \tag{A2}$$

Table A1. Point coordinates under prescribed motion.

DOF	Surge	Sway	Heave	Roll	Pitch	Yaw
$x(t)$	p	0	0	0	$L_2 + L_\mathrm{e}\sin(p-\alpha_\mathrm{e}) + R\sin(p)\cos(\theta)$	$R\sin(\theta)\sin(p) + L_2(1-\cos(p))$
$y(t)$	$-R\sin(\theta)$	$p - R\sin(\theta)$	$-R\sin(\theta)$	$-L_1\sin(p) - R\sin(\theta+p)$	$-R\sin(\theta)$	$-R\sin(\theta)\cos(p) - L_2\sin(p)$
$z(t)$	$z_\mathrm{rc} + R\cos(\theta)$	$z_\mathrm{rc} + R\cos(\theta)$	$p + z_\mathrm{rc} + R\cos(\theta)$	$z_\mathrm{p} + L_1\cos(p) + R\cos(\theta+p)$	$z_\mathrm{p} + L_\mathrm{e}\cos(p-\alpha_\mathrm{e}) + R\cos(p)\cos(\theta)$	$z_\mathrm{rc} + R\cos(\theta)$

where $\Delta x_i|_\mathrm{sim}$ is the dimensional simulation displacement, $\Delta x_i|_\mathrm{theo}$ is the dimensional theoretical displacement, and A_pp is the dimensional point motion amplitude caused by the prescribed motion exclusively, i.e., as if the rotor was not rotating. The subscript "pp" stands for "prescribed point". This way, the motion prescription error was measured relative to the prescribed amplitude. The dimensional point motion amplitudes are summarized in Table A2. For surge, sway and heave, they are simply the prescribed motion amplitude. For roll and pitch, they represent the motion amplitude (in length units) of a point at radial distance R from the rotor center, and $\theta(t) = 0$ deg (i.e., assuming the rotor is not rotating). For yaw, the same is true but assuming an azimuth $\theta(t) = 90$ deg instead. The validation was done for the point at $82\ \%$ of the span with an initial azimuth of 0 deg.

Table A2. Point motion amplitudes caused by the prescribed motion exclusively.

Cases	Surge	Sway	Heave	Roll	Pitch	Yaw
A_pp	A_p	A_p	A_p	$A_\mathrm{p}(L_1+R)$	$A_\mathrm{p}\sqrt{(L_1+R)^2+L_2^2}$	$A_\mathrm{p}\sqrt{L_2^2+R^2}$

Figure A1 compares the theoretical (blue) and simulation (black) coordinate values for the PiLS, PiHS, SwHS and YaHS cases. The relative error is shown in red. Each column represents one case. The rows represent the coordinates affected by the prescribed motion (e.g., x and z for pitch). It can be seen that the prescribed motion closely follows the theoretical prediction, as observed across all cases, including the ones not shown. The PiHS, SwHS and YaHS cases showed the largest errors of all cases. Although not completely shown, all the low-St_p/high-A_p^* cases showed errors very close to 0%. The largest errors occurred for the high-St_p/low-A_p^* cases, but they were nevertheless below 3.75% of the prescribed motion amplitude at the given point. This small mismatch can be explained by the fact that the prescribed motion is obtained through velocity prescription, which leads to integration errors and some lag. We support this argument by noting that the errors tend to be larger when the slope of the curves is higher, i.e., when the structural velocity is higher.

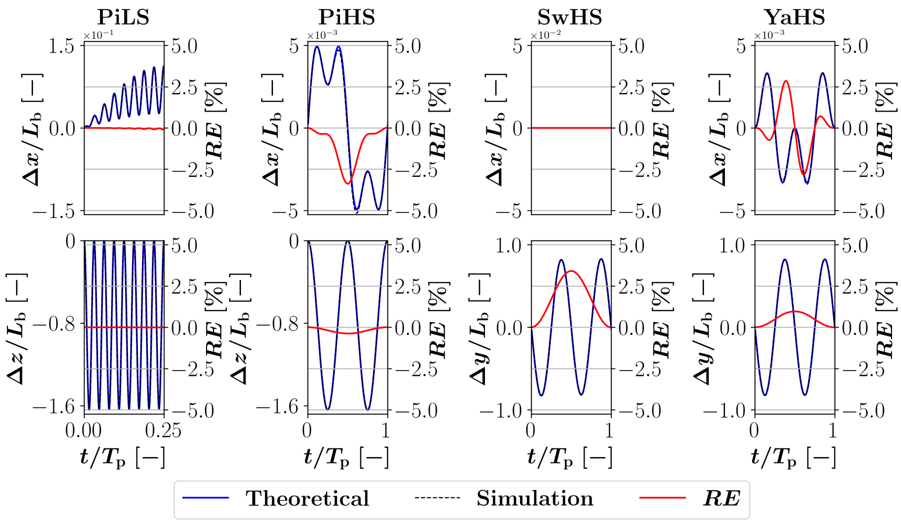

Figure A1. Point motion theoretical prediction and simulation output. The time was normalized by the prescribed motion period $T_\mathrm{p} = 1/f_\mathrm{p}$.

Appendix B: Flow field convergence

The flow field time convergence was assessed with the forward-moving average of the streamwise velocity component defined by:

$$\frac{<U_x>}{U_0}(t) = \frac{<U_x>|_t^{t+\Delta t}}{U_0} \tag{B1}$$

and the forward-moving standard deviation, defined by:

$$\frac{<U_x'^2>^{1/2}}{U_0}(t) = \frac{<U_x'^2>^{1/2}|_t^{t+\Delta t}}{U_0}\ , \tag{B2}$$

where $<\cdot>$ denotes the time average performed in the interval $[t, t+\Delta t]$, and $U_x' = U_x - <U_x>$. The simulations were performed for a period of time $T_\mathrm{sim} = 64$ s, such that the flow traversed the domain from the inlet to the end of the wake refinement region 8.6 times. This time interval was also equal to eight periods of the lowest simulated frequency. The distance from the inlet to the end of the wake refinement region was equal to $12.5D$. The averaging time interval Δt was equal to one prescribed motion period of the lowest simulated frequency ($\Delta t = T_\mathrm{lp} = 8$ s).

Figures B1 and B2 show the streamwise velocity in black, the forward-moving average in blue and the forward-moving standard deviation in green for the SwLS and SwHS cases, respectively. The first row represents streamwise positions located at the rotor centerline. The second row represents streamwise positions located one rotor radius above the centerline. Each column corresponds to a streamwise location. The SwLS case showed reasonable convergence of the statistics at $t_\mathrm{conv} = 4T_\mathrm{lp} = 32$ s (red dashed line), as did the SwHS case. Although not shown here, all cases showed similar convergence plots and were deemed converged at $t_\mathrm{conv} = 32$ s. Therefore, the time interval from 32 s to 64 s was used for computing the statistics shown in this manuscript.

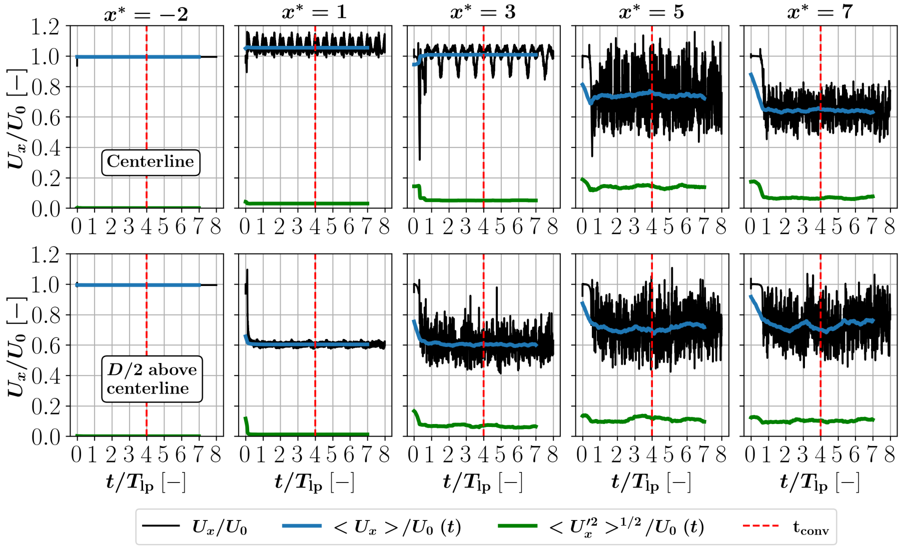

Figure B1. Streamwise flow velocity convergence for the SwLS case. The streamwise velocity is shown in black. The forward-moving average is shown in blue. The forward-moving standard deviation is shown in green. The first row represents streamwise positions located at the rotor centerline. The second row represents streamwise positions located one rotor radius above the centerline.

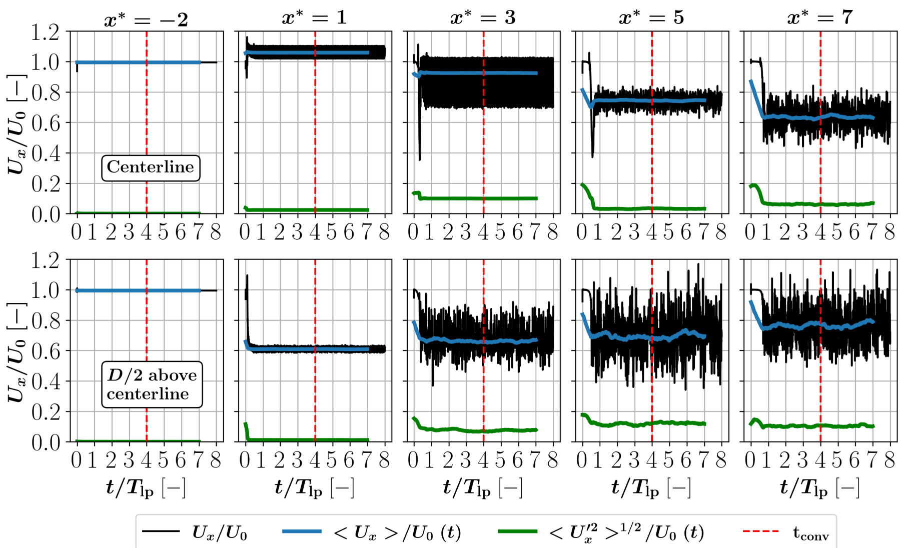

Figure B2. Streamwise flow velocity convergence for the SwHS case. The streamwise velocity is shown in black. The forward-moving average is shown in blue. The forward-moving standard deviation is shown in green. The first row represents streamwise positions located at the rotor centerline. The second row represents streamwise positions located one rotor radius above the centerline.

Appendix C: Experimental comparison

Some cases were compared to the experimental data available in Bergua et al. (2023) and Fontanella et al. (2021a, b). An extensive comparison between these experimental data and the results of many participants was carried out with a focus on the loads in Bergua et al. (2023), and a focus on the wake in Cioni et al. (2023). Wake results for a setup similar to the one used in this manuscript are included in Cioni et al. (2023).

This appendix compares the rotor loads of the FB, SuLS, SuHS, PiLS and PiHS cases against the experimental data. Two experiments were performed. Experiment 1 covered the surge cases, and Experiment 2 repeated the surge cases, while adding the pitch cases. In general, Experiment 1 showed less variation in the time-averaged aerodynamic forces, indicating more reliable results (Bergua et al., 2023). Experiment 2 may have had some interference due to some factors including the use of a different rotor speed controller that resulted in some rotor speed oscillations, the influence of the cable bundle used for the sensors and power located behind the wind turbine, and a small blade pitch angle offset (Bergua et al., 2023). Hence, cases FB, SuLS and SuHS come from Experiment 1, while the remaining cases come from Experiment 2. The cases at 2 Hz (SuHS and PiHS) were reported to have higher uncertainty in the measurements associated with the inertial loads and should be evaluated cautiously (Bergua et al., 2023).

The experimental comparison was made in terms of time average, amplitude of oscillation and phase shift. For the experimental cases, the time-averaged value was taken over the full length of the time series. The amplitude and phase shift were obtained from the FFT spectrum of a section of the time series. This section was the largest section possible such that the frequency step was a submultiple of the prescribed motion frequency. This fact, together with the use of a flat-top window, reduced spectral leakage and provided the highest amplitude accuracy. The simulation data was post-processed in the same way as the experimental data, and the data was taken between $t = 32$ s and $t = 64$ s.

Figure C1 shows the thrust T (top row) and torque M (bottom row) comparisons. The first column addresses the time-averaged load value (denoted by $< \cdot >$), the second column addresses the amplitude of oscillation (denoted by $\cdot'$), and the third column addresses the phase shift between the prescribed motion and the load ($\phi_\mathrm{p} - \phi_\mathrm{i}$, where $i \in \{T, M\}$). The modulus of the difference relative to the experimental value is denoted by $|RE|$. In terms of time-averaged value, the simulations differed from the experimental results by at most 8% and 13% for thrust and torque, respectively. Worse results for torque were expected, since the turbine was designed to match the C_T curve, not the C_P curve. Differences in the load amplitudes for the SuLS and PiLS cases were below 10%. Some of the error in the amplitude of variation should be related to the error in the time-averaged value, since the amplitude of variation should scale with the time-averaged value, according to the quasi-steady theory (Fontanella et al., 2021b, 2022). The larger mismatch in amplitudes of the SuHS and PiHS cases was attributed to the higher uncertainty in the measurements associated with the inertial loads. Moreover, the amplitude in the experimental data of PiHS (0.26 deg) was about 13.3% lower than in the load case definition (0.3 deg). As for the phase difference between the motion and the loads, there was a reasonable agreement between the simulation and the experimental results.

Some differences between the simulation setup and the experiments were present. These include: modeling the inflow with no shear, when there was slight shear in the rotor area in the experiments; the lack of turbulence in the simulations, when the

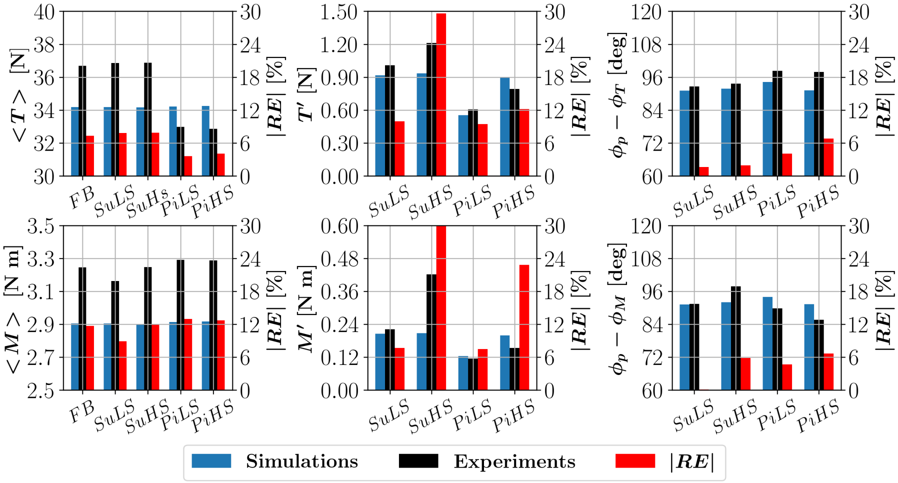

Figure C1. Thrust and torque comparison between simulations and UNAFLOW experiments.

inflow in the experiments had a 2% turbulence intensity; and modeling the walls as slip walls with no boundary layer, when there was actually boundary layer growth in the wind tunnel. The authors recognize that the simulation setup did not exactly match the experimental setup, but would like to note that there were technical limitations and uncertainties in the experiments that may have exacerbated the mismatches. In terms of the simulations, another important factor impacting the results was the high sensitivity that the actuator-line model has to the smearing length scale ϵ and the cell size Δx, as small changes in these parameters can lead to large changes in the loads. This has been widely reported in the literature (Mikkelsen, 2003; Troldborg et al., 2009; Martínez-Tossas et al., 2015, 2017; Amaral et al., 2024). In particular, Amaral et al. (2024) demonstrated that the cell size increase at the rotor center due to the addition of a geometry-resolved nacelle in the fixed-bottom simulation performed in this manuscript was enough to meaningfully improve the match with the experiment. The high sensitivity that the actuator-line model has to the smearing length scale and cell size can be overcome by implementing model corrections (Meyer Forsting et al., 2019; Martínez-Tossas and Meneveau, 2019). However, due to time restrictions, it was not possible to explore the topic further, and a uniform value of $\epsilon/\max(\Delta x) = 2$ (Troldborg et al., 2009) was used, where $\max(\Delta x)$ is the maximum cell size in the vicinity of the rotor.

. All simulation data are available upon request. Commercial licenses for YALES2 can be purchased from Laboratoire CORIA.

. RA performed the simulations, post-processing and was responsible for writing the manuscript. FHM provided indispensable support in handling the simulation tool, provided text excerpts, references and some figures. All the authors provided valuable input and insights that were important to steer the work and write the manuscript. PD and AV were crucial in providing the necessary resources to produce this work.

. RA, DvT and AV declare that they have no conflict of interest. FHM, KL and PD declare that they were full-time employees of Siemens Gamesa Renewable Energy at the time this work was carried out.

. This work results from the STEP4WIND project, a European Doctorate programme granted under the H2020 Marie-Curie Innovative Training Network (H2020-MSCA-ITN-2019, grant 860737.) We thank SURF (www.surf.nl) for the use of the National Supercomputer Snellius. This work is part of W2ITASEC (Wind turbine Wake Interactions through Aero-Servo-Elastic Coupling) with computer resources provided by GENCI at TGCC (grant 2023-S142aspe00038 on the supercomputer Joliot Curie). The authors acknowledge the use of computational resources of the DelftBlue supercomputer, provided by Delft High Performance Computing Centre (https://www.tudelft.nl/dhpc). We would like to thank Roger Bergua and Alessandro Fontanella for providing information regarding the experimental setup used to benchmark the simulations.

References

Ainslie, J. F.: Calculating the flowfield in the wake of wind turbines, Journal of Wind Engineering and Industrial Aerodynamics, 27, 213–224, 1988.

Amaral, R., Houtin-Mongrolle, F., von Terzi, D., and Viré, A.: Nacelle modeling considerations for wind turbines using large-eddy simulations, J. Phys.: Conf. Ser., 2767, https://doi.org/10.1088/1742-6596/2767/5/052056, 2024.

Bak, C., Zahle, F., Bitsche, R., Kim, T., Yde, A., Henriksen, L. C., Hansen, M. H., Blasques, J. P., Gaunaa, M., and Natarajan, A.: The DTU 10-MW reference wind turbine, Tech. rep., Danish Wind Power Research, available at: http://orbit.dtu.dk/files/55645274/The_DTU_10MW_Reference_Turbine_Christian_Bak.pdf, 2013.

Barooni, M., Ashuri, T., Velioglu Sogut, D., Wood, S., , and Ghaderpour Taleghani, S.: Floating Offshore Wind Turbines: Current Status and Future Prospects, Energies, 16, https://doi.org/10.3390/en16010002, 2023.

Bastankhah, M. and Porté-Agel, F.: A new analytical model for wind-turbine wakes, Renew. Energy, 70, 116–123, https://doi.org/10.1016/j.renene.2014.01.002, 2014.

Bayati, I., Belloli, M., Bernini, L., and Zasso, A.: Aerodynamic design methodology for wind tunnel tests of wind turbine rotors, Journal of Wind Engineering and Industrial Aerodynamics, 167, 217–227, https://doi.org/10.1016/j.jweia.2017.05.004, 2017.

Benard, P., Viré, A., Moureau, V., Lartigue, G., Beaudet, L., Deglaire, P., and Bricteux, L.: Large-Eddy Simulation of wind turbines wakes including geometrical effects, Computers and Fluids, 173, 133–139, https://doi.org/10.1016/j.compfluid.2018.03.015, 2018.

Bergua, R., Robertson, A., Jonkman, J., Branlard, E., Fontanella, A., Belloli, M., Schito, P., Zasso, A., Persico, G., Sanvito, A., Amet, E., Brun, C., Campaña-Alonso, G., Martín-San-Román, R., Cai, R., Cai, J., Qian, Q., Maoshi, W., Beardsell, A., Pirrung, G., Ramos-García, N., Shi, W., Fu, J., Corniglion, R., Lovera, A., Galván, J., Nygaard, T. A., dos Santos, C. R., Gilbert, P., Joulin, P.-A., Blondel, F., Frickel, E., Chen, P., Hu, Z., Boisard, R., Yil-mazlar, K., Croce, A., Harnois, V., Zhang, L., Li, Y., Aristondo, A., Mendikoa Alonso, I., Mancini, S., Boorsma, K., Savenije, F., Marten, D., Soto-Valle, R., Schulz, C. W., Netzband, S., Bianchini, A., Papi, F., Cioni, S., Trubat, P., Alarcon, D., Molins, C., Cormier, M., Brüker, K., Lutz, T., Xiao, Q., Deng, Z., Haudin, F., , and Goveas, A.: OC6 project Phase III: validation of the aerodynamic loading on a wind turbine rotor undergoing large motion caused by a floating support structure, Wind Energ. Sci., 8, 465–485, https://doi.org/10.5194/wes-8-465-2023, 2023.

Chamorro, L. P. and Porté-Agel, F.: Effects of thermal stability and incoming boundary-layer flow characteristics on wind-turbine wakes: a wind-tunnel study, Bound.-Lay. Meteorol., 136, 515-533, https://doi.org/10.1007/s10546-010-9512-1, 2010.

Chamorro, L. P., Hill, C., Morton, S., Ellis, C., Arndt, R. E. A., and F, S.: On the interaction between a turbulent open channel flow and an axial-flow turbine, J. Fluid Mech., 716, 658-670, https://doi.org/10.1017/jfm.2012.571, 2013.

Cioni, S., Papi, F., Pagamonci, L., Bianchini, A., Ramos-García, N., Pirrung, G., Corniglion, R., Lovera, A., Galván, J., Boisard, R., Fontanella, A., Schito, P., Zasso, A., Belloli, M., Sanvito, A., Persico, G., Zhang, L., Li, Y., Zhou, Y., Mancini, S., Boorsma, K., Amaral, R., Viré, A., Schulz, C. W., Netzband, S., Soto-Valle, R., Marten, D., Martín-San-Román, R., Trubat, P., Molins, C., Bergua, R., Branlard, E., Jonkman, J., , and Robertson, A.: On the characteristics of the wake of a wind turbine undergoing large motions caused by a floating structure: an insight based on experiments and multi-fidelity simulations from the OC6 project Phase III, Wind Energ. Sci., 8, 1659–1691, https://doi.org/10.5194/wes-8-1659-2023, 2023.

Cioni, S., Papi, F., Balduzzi, F., Fontanella, A., and Bianchini, A.: Blade-resolved CFD analysis of a floating wind turbine: new insights on unsteady aerodynamics, loads, and wake, Ocean Engineering, 341, 122 746, 2025.

Costanzo, G., Brindley, G., O'Sullivan, R., de Velde, L. V., and Bickley, J.: Latest wind energy data for Europe: Autumn 2024, Tech. rep., Wind Europe, available at: https://windeurope.org/intelligence-platform/product/latest-wind-energy-data-for-europe-autumn-2024/#overview, 2024.

Cozzi, L., Wanner, B., Donovan, C., Toril, A., Yu, W., Arsalane, Y., D'Ambrosio, D., Liu, J., Papapanagiotou, S., Pavarini, C., Perugia, D., Staas, L., Waldron, M., Gould, T., Hosker, E., Justus, D., Coon, T., Santos, M. D., and Tsoukala, E.: Offshore Wind Outlook 2019, World Energy Outlook Special Report, Tech. rep., International Energy Agency, available at: https://www.iea.org/reports/offshore-wind-outlook-2019, 2019.

De Cillis, G., Cherubini, S., Semeraro, O., Leonardi, S., and De Palma, P.: POD-based analysis of a wind turbine wake under the influence of tower and nacelle, Wind Energ., 24, 609–633, https://doi.org/10.1002/we.2592, 2020.

Firpo, A., Sanvito, A. G., Persico, G., and Dossena, V.: Actuator line URANS-to-LES comparison of single and tandem floating offshore wind turbines, Wind Energy Science, 11, 557–584, 2026.

Fontanella, A., Bayati, I., Mikkelsen, R., Belloli, M., and Zasso, A.: UNAFLOW: UNsteady Aerodynamics of FLOating Wind turbines, Zenodo [data set], 173, 133–139, https://doi.org/10.5281/zenodo.4740006, 2021a.

Fontanella, A., Bayati, I., Mikkelsen, R., Belloli, M., and Zasso, A.: UNAFLOW: a holistic wind tunnel experiment about the aerodynamic response of floating wind turbines under imposed surge motion, Wind Energ. Sci., 6, 1169–1190, https://doi.org/10.5194/wes-6-1169-2021, 2021b.

Fontanella, A., Facchinetti, A., Di Carlo, S., and Belloli, M.: Wind tunnel investigation of the aerodynamic response of two 15 MW floating wind turbines, Wind Energy Science Discussions, 2022, 1–25, 2022.

Fontanella, A., Fusetti, A., Cioni, S., Papi, F., Muggiasca, S., Persico, G., Dossena, V., Bianchini, A., and Belloli, M.: Wake development in floating wind turbines: New insights and open dataset from wind tunnel experiments, Wind Energy Science Discussions, 2024, 1–23, 2024.

Fontanella, A., Cioni, S., Papi, F., Muggiasca, S., Bianchini, A., and Belloli, M.: Experimental investigation of the effects of floating wind turbine motion on a downstream turbine performance and loads, Wind Energy Science Discussions, 2025, 1–29, 2025.

Germano, M., Piomelli, U., Moin, P., and Cabot, W. H.: A dynamic subgrid-scale eddy viscosity model, Phys. Fluids, 3, 1760–1765, https://doi.org/10.1063/1.857955, 1990.

Gupta, V. and Wan, M.: Low-order modelling of wake meandering behind turbines, Journal of Fluid Mechanics, 877, 534–560, 2019.

Heisel, M., Hong, J., and Guala, M.: The spectral signature of wind turbine wake meandering: A wind tunnel and field-scale study, Wind Energy, 21, 683–806, https://doi.org/10.1002/we.2189, 2018.

Hodgson, E. L., Madsen, M. H. A., and Andersen, S. J.: Effects of turbulent inflow time scales on wind turbine wake behavior and recovery, Physics of Fluids, 35, 2023.

Houtin-Mongrolle, F.: Investigations of yawed offshore wind turbine interactions through aero-servo-elastic Large Eddy Simulations, Ph.D. thesis, INSA Rouen Normandie, https://theses.hal.science/tel-03987411v1/document, 2022.

Howard, K. B., Singh, A., F, S., and Guala, M.: On the statistics of wind turbine wake meandering: an experimental investigation, Phys. Fluids, 27, 369-380, https://doi.org/10.1017/jfm.2014.174, 2015.

Jensen, N.: A note on wind generator interaction, no. 2411 in Risø-M, Risø National Laboratory, ISBN 87-550-0971-9, 1983.

Kang, S., Yang, X., and Sotiropoulos, F.: On the onset of wake meandering for an axial flow turbine in a turbulent open channel flow, J. Fluid Mech., 744, 376–403, https://doi.org/10.1017/jfm.2014.82, 2014.

Katic, I., Hojstrup, J., and Jensen, N. O.: A simple model for cluster efficiency, in: Proceedings from the European Wind Energy Conference, pp. 407–410, Rome, Italy, 1986.

Kraushaar, M.: Application of the compressible and low-Mach number approaches to Large-Eddy Simulation of turbulent flows in aero-engines, Ph.D. thesis, INPT, https://theses.hal.science/file/index/docid/711480/filename/Kraushaar_.pdf, 2011.

Larsen, G. C.: A simple stationary semi-analytical wake model, Risø National Laboratory for Sustainable Energy, 2009.

Larsen, G. C., Madsen Aagaard, H., Bingöl, F., Mann, J., Ott, S., Sørensen, J. N., Okulov, V., Troldborg, N., Nielsen, N. M., Thomsen, K., Larsen, T. J., and Mikkelsen, R.: Dynamic wake meandering modeling, Risø National Laboratory, https://doi.org/10.1016/j.renene.2014.01.002, 2007.

Li, Y., Yu, W., and Sarlak, H.: Wake structures and performance of wind turbine rotor with harmonic surging motions under laminar and turbulent inflows, Wind Energy, 27, 1499–1525, 2024.

Li, Z., Dong, G., and Yang, X.: Onset of wake meandering for a floating offshore wind turbine under side-to-side motion, J. Fluid Mech., 934, https://doi.org/10.1017/jfm.2021.1147, 2022.

Lignarolo, L., Ragni, D., Scarano, F., Ferreira, C., and Bussel, G.: Tip-vortex instability and turbulent mixing in wind-turbine wakes, J. Fluid Mech., 781, 467–493, https://doi.org/10.1017/jfm.2014.82, 2015.

Mao, X. and Sørensen, J. N.: Far-wake meandering induced by atmospheric eddies in flow past a wind turbine, J. Fluid Mech., 846, 190–209, https://doi.org/10.1017/jfm.2018.275, 2018.

Martínez-Tossas, L., Churchfield, M., and Leonardi, S.: Large eddy simulations of the flow past wind turbines: actuator line and disk modeling, Wind Energy, 18, 1047–1060, https://doi.org/10.1002/we.1747, 2015.

Martínez-Tossas, L., Churchfield, M., and Meneveau, C.: Optimal Smoothing Length Scale for Actuator Line Models of Wind Turbine Blades Based on Gaussian Body Force Distribution, Wind Energy, 20, 1083–1096, https://doi.org/10.1002/we.2081, 2017.

Martínez-Tossas, L. A. and Meneveau, C.: Filtered lifting line theory and application to the actuator line model, J. Fluid Mech., 863, 269–292, https://doi.org/10.1017/jfm.2018.994, 2019.

Medici, D.: Experimental studies of wind turbine wakes: power optimisation and meandering, Ph.D. thesis, KTH, https://www.mech.kth.se/thesis/2006/phd/phd_2006_davide_medici.pdf, 2005.

Medici, D. and Alfredsson, P. H.: Measurements on a Wind Turbine Wake: 3D Effects and Bluff Body Vortex Shedding, Wind Energ., 9, 219–236, https://doi.org/10.1002/we.156, 2006.

Messmer, T., Hölling, M., and Peinke, J.: Enhanced recovery caused by nonlinear dynamics in the wake of a floating offshore wind turbine, J. Fluid Mech., 984, https://doi.org/10.1017/jfm.2024.175, 2024.

Messmer, T., Peinke, J., Croce, A., and Hölling, M.: The role of motion-excited coherent structures in improved wake recovery of a floating wind turbine, Journal of Fluid Mechanics, 1018, A23, 2025.

Meyer Forsting, A. R., Pirrung, G. R., and Ramos-García, N.: A vortex-based tip/smearing correction for the actuator line, Wind Energ. Sci., 4, 369–383, https://doi.org/10.5194/wes-4-369-2019, 2019.

Mian, H., Messmer, T., Stoevesandt, B., and Siddiqui, M.: Coherent flow structures in the wake of a model floating wind turbine under pitch and roll motions, Energy, p. 138212, 2025.

Mikkelsen, R.: Actuator Disc Methods Applied to Wind Turbines, Ph.D. thesis, Technical University of Denmark, https://backend.orbit.dtu.dk/ws/portalfiles/portal/5452244/Robert.PDF, 2003.

Moureau, V., Domingo, P., and Vervisch, L.: Design of a massively parallel CFD code for complex geometries, Comptes Rendus Mécanique, 339, 1239–1250, https://doi.org/10.1016/j.crme.2010.12.001, 2011.

Okulov, V. L., Naumov, I. V., Mikkelsen, R. F., Kabardin, I. K., and N, S. J.: A regular Strouhal number for large-scale instability in the far wake of a rotor, J. Fluid Mech., 747, 369-380, https://doi.org/10.1017/jfm.2014.174, 2014.

Pagamonci, L., Papi, F., Cojocaru, G., Belloli, M., and Bianchini, A.: How does turbulence affect wake development in floating wind turbines? Some insights from comparative large-eddy simulations and wind tunnel experiments, Wind Energy Science, 10, 1707–1736, 2025.

Sorensen, J. N. and Shen, W. Z.: Numerical modeling of wind turbine wakes, J. Fluids Eng., 124, 393–399, 2002.

Troldborg, N., Sørensen, J., and Mikkelsen, R.: Actuator Line Modeling of Wind Turbine Wakes, Ph.D. thesis, Technical University of Denmark, https://backend.orbit.dtu.dk/ws/files/5289074/Thesis.pdf, 2009.

WindEurope: Europe can expect to have 10 GW of floating wind by 2030, https://windeurope.org/newsroom/news/europe-can-expect-to-have-10-gw-of-floating-wind-by-2030/, 2022.